2014

Evaluation of the Design of Komendant's Cycloidal, Thin Shell Roofs At the Kimbell Art Museum Using Finite Element Analysis

Mikhail Osanov
Bucknell University, mo018@bucknell.edu

Follow this and additional works at: https://digitalcommons.bucknell.edu/honors_theses

EVALUATION OF THE DESIGN OF KOMENDANT'S CYCLOIDAL, THIN SHELL ROOFS AT THE KIMBELL ART MUSEUM USING FINITE ELEMENT ANALYSIS
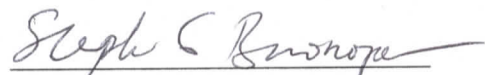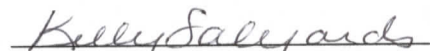
by

Mikhail Osanov

A Proposal Submitted to the Honors Council

For Honors in Department of Civil Engineering

Date: 05/01/14

Approved by:

Adviser: Stephen Buonopane

Co-Adviser: Kelly Salyards

Acknowledgements

I would like to express my deepest appreciation to my adviser, Professor Stephen Buonopane, who gave me an opportunity to assist him with summer research, which resulted in my thesis. Your advice and comments on research as well as on my career have always been insightful and valuable and the experience that I acquired thanks to you will help me succeed in my future pursuit of a PhD at Johns Hopkins University. Without your guidance and persistent help, this thesis would not have been possible.

I would also like to thank my co-adviser, Professor Kelly Salyards. You have always encouraged me in my pursuit of further education and provided invaluable advice and comments on my research and career decisions. Thank you for keeping your door open and helping me succeed in my undergraduate career.

Finally, I would like to thank Professor Sharon Garthwaite from the Department of Mathematics, Professor Salyards and Professor Buonopane for serving on the defense committee and letting my honors defense be an enjoyable moment.

Table of Contents

List of Tables

List of Figures

Abstract

The analysis of Komendant's design of the Kimbell Art Museum was carried out in order to determine the effectiveness of the ring beams, edge beams and prestressing in the shells of the roof system. Finite element analysis was not available to Komendant or other engineers of the time to aid them in the design and analysis. Thus, the use of this tool helped to form a new perspective on the Kimbell Art Museum and analyze the engineer's work. In order to carry out the finite element analysis of Kimbell Art Museum, ADINA finite element analysis software was utilized. Eight finite element models (FEM-1 through FEM-8) of increasing complexity were created. The results of the most realistic model, FEM-8, which included ring beams, edge beams and prestressing, were compared to Komendant's calculations. The maximum deflection at the crown of the mid-span surface of -0.1739 in. in FEM-8 was found to be larger than Komendant's deflection in the design documents before the loss in prestressing force (-0.152 in.) but smaller than his prediction after the loss in prestressing force (-0.3814 in.). Komendant predicted a larger longitudinal stress of -903 psi at the crown (vs. -797 psi in FEM-8) and 37 psi at the edge (vs. -347 psi in FEM-8). Considering the strength of concrete of 5000 psi, the difference in results is not significant. From the analysis it was determined that both FEM-5, which included prestressing and fixed rings, and FEM-8 can be successfully and effectively implemented in practice. Prestressing was used in both models and thus served as the main contribution to efficiency. FEM-5 showed that ring and edge beams can be avoided, however an architect might find them more aesthetically appropriate than rigid walls.

Chapter 1: Introduction

August Komendant (1906-1992), an Estonian and American structural engineer, was a pioneer in the field of reinforced concrete and the applications of post-tensioning and pre-stressing. In collaboration with the architect Louis Kahn, he was the structural engineer for buildings such as the Salk Institute for Biological Studies in San Diego, California, Richards Medical Research Laboratories in Philadelphia, Pennsylvania, and Kimbell Art Museum in Fort Worth, Texas. All these buildings were the product of a close collaboration of architect and structural engineer, which is not often the case in modern structures (Charleson & Pirie, 2009).

The Kimbell Art Museum, 1972 (Figure 1) is of particular interest to architects and engineers because of its aesthetic quality and structural honesty.

**Figure 1. Images of the thin shell roofs of the Kimbell Art Museum
(Highsmith, 2011) (Praefcke, 2009)**

The museum is also very unique from the structural engineering point of view. As shown in Figure 2, Kimbell Art Museum consists of a series of interconnected cycloidal barrel shells. The most typical units are 104 ft. long and consist of a 100 ft. cycloidal shell, 2 ft.

wide ring beams on each end and edge beams stretching along both sides. The structure of the museum also consists of several short shells, which are 30 ft., 49 ft. and 38 ft. long, which are important from an architectural point of view in terms of organization of space. Komendant applies post-tensioning within the curved surface of each shell to achieve the span required for each shell.
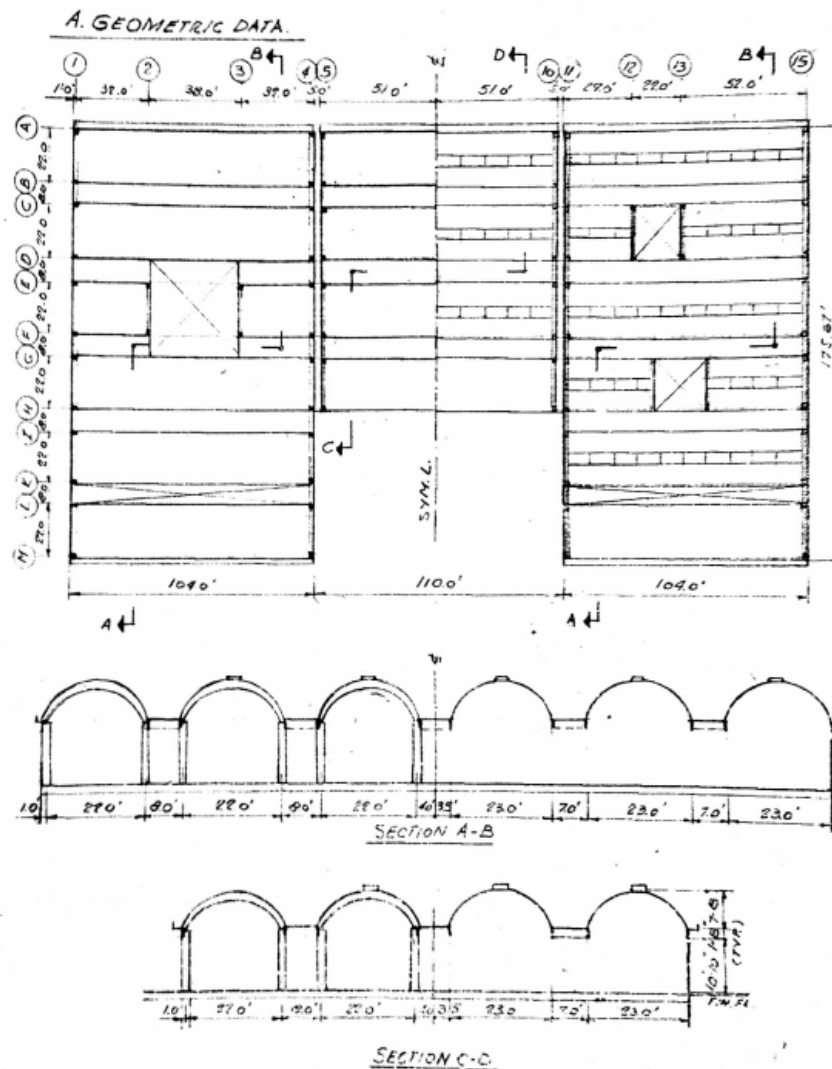
Figure 2. Plan and elevation view of the Kimbell Art Museum (Komendant, 1970 p.1).

Initially, Kahn proposed using angular vaults of folded plates as shown in Figure 3 (Leslie, 2005).
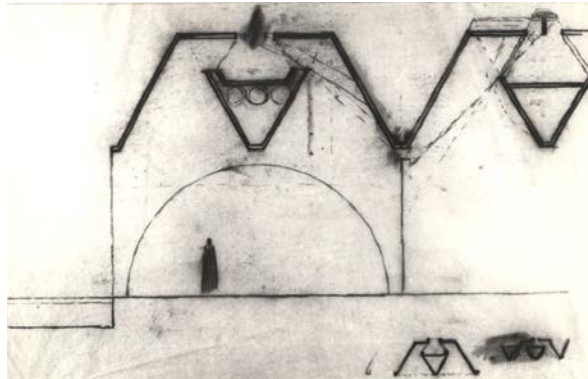
Figure 3. Initial design of Kimbell Art Museum (University of Pennsylvania, 2009)

However, Richard Fargo Brown, who, at the time, was hired to be the founding director of the museum, rejected this design. The folded plate design required the ceiling to be 30 ft. high, which was higher than he envisioned (Leslie, 2005). Several other options were considered. In June of 1967, Kahn suggested using semicircular ceiling, which Brown found "ostentatious and thus, dictated by its geometry, too high" (Leslie, 2005). Kahn also proposed using a flattened arch, which met the requirements of the overall height but wasn't "particularly graceful" (Leslie, 2005). Other solutions included a flat roof with quarter-round edges, ellipses and segmented circles but none of them were accepted (Leslie, 2005). Finally, the research carried out by Marshall Meyers, Kahn's project architect, revealed that the use of a cycloid curve would reduce the ceiling height and produce a very appealing diffusion of natural and artificial light from the skylight running along the apex of several cycloids as shown in Figure 4 (Kimbell Art Museum, 2014).

The diffusion of light was critical because it provided illumination and did not harm the paintings (Kimbell Art Museum, 2014).

Figure 4. Skylight along the top of the shell ("Bess of both," 2013)

In order to provide continuity across the skylight openings, concrete struts were inserted at 10 ft. intervals parallel to the shell's cross-section. Earlier cylindrical barrel shells such as those by the German structural engineer Franz Dischinger (1887 – 1953) (Figure 5) used stiff walls to restrain the free edges of the shell, which allowed them to use simpler analytical methods. At that time analytical methods were limited in terms of computational power, but this limit did not set any constraints on their creativity and imagination in pursuit of efficient forms. Finite element (FE) computer modeling of structures now allows more detailed analysis of complicated structural forms. Thus, a study of Komendant's original design documents will be carried out along with the finite element analysis of the structure and a criticism of the built work.

Figure 5. Dischinger shell loaded by the Dyckerhoff and Widmann engineers in 1932 in Weisbaden-Biebrich, Germany (Hines & Billington, 2004)

Chapter 2: Problem Statement

As mentioned in Billington (1976) "Historical Perspective on Prestressed Concrete," "the idea of prestressing, a product of the twentieth century, announced the single most significant new direction in structural engineering of any period in history". Prestressed concrete revealed new possibilities of form, with potential for great visual appeal, and required the collaboration of architects and engineers. Louis Kahn, the architect of the Kimbell Art Museum recognized this technique as the means to fulfill his goals and ideas through a close collaboration with August Komendant. Komendant was not the only engineer who used prestressing in his design of concrete shells in the same timeframe as the Kimbell Art Museum. For example, a giant post-tensioned hyperbolic paraboloid (hypar) shell for Ponce Celiseum in Puerto Rico was completed in 1971, just one year before Kimbell was constructed (Lin, Kulka & Lo, 1973).

Finite element analysis was not available to Komendant or other engineers of the time to aid them in design and analysis. Thus, the use of finite element analysis will help to provide a new perspective on the Kimbell Art Museum and help to analyze the engineer's work. In the design of the structure, Komendant did not rely on solid walls for support as early shell designers did, but rather stiffened his shells with the use of ring and edge beams as shown in Figure 6 and increased strength by using prestressing cables running along the length of the shells. In fact, he had to avoid using rigid walls because the museum had to have uninterrupted space and said walls would interfere with the desired architectural style. The analysis of Komendant's design was carried out with the

intention to determine the effectiveness of the ring beams, edge beams and prestressing in the Kimbell shells.

Thus, several models of various complexities were built in ADINA using 3D solid elements, truss elements and plate elements. The simplest models include just the cycloid without stiffening but with various boundary constraints. More complex models include end and edge stiffening and prestressing. To simplify the problem, an assumption was made that the concrete struts in the skylight provide enough rigidity to the structure for it to behave similar to having no skylight, and thus the skylight was not included in the models. The results are compared to Komendant's calculations and presented in the subsequent chapters.

Table 1 summarizes the models that were created using ADINA, as well as the number of equations that were assembled for each model. "Free" indicates that the selected boundary is free to displace or rotate in any axis, "fixed" indicates that the selected boundary is restrained from displacement and rotation in all axes. The presence or absence of prestressing is indicated by "yes" or "no", while "beam" indicates the presence of the ring or edge beam. The development of the models was guided by the goal to evaluate the efficiency of ring and edge support conditions and prestressing.

Table 1. Description of models that were created and studied using ADINA.

FE model	Edge	Ring	Prestressing	Number of Equations
FEM-1	Free	Free	No	2,855,103
FEM-2	Free	Free	Yes	2,855,103
FEM-3	Fixed	Free	No	2,821,731
FEM-4	Free	Fixed	No	2,844,977
FEM-5	Free	Fixed	Yes	2,844,977
FEM-6	Fixed	Fixed	No	2,811,741
FEM-7	Beam	Beam	No	6,066,848
FEM-8	Beam	Beam	Yes	6,066,848

FEM-8 represents the most realistic representation of the as-built structure, which can be compared to Komendant's design calculations as well as with the simpler FEM models.

Chapter 3: Development of FEM Model

3.1 Cycloid Geometry

The structure under consideration is a cycloidal shell between the centerlines of the edge beams as shown in Figure 6.
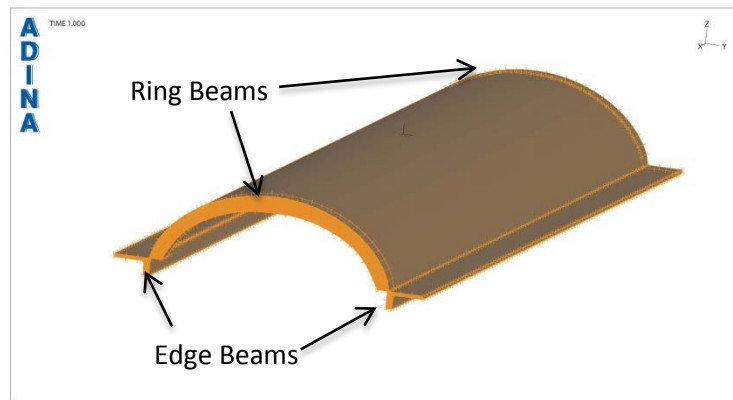
Figure 6. ADINA model of the cycloidal shell under consideration

A cycloid is a geometric shape, which is represented by the path traced out by a fixed point of a circle rotating along straight path as shown in Figure 7.
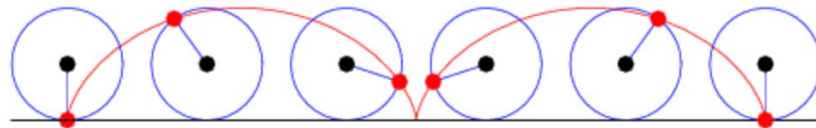
Figure 7. Formation of a cycloid by a fixed point of a rotating circle (Wolfram Mathworld, 2014).

A cycloid is defined by the following equations:

$$y = r(\theta - \sin\theta) \hspace{3cm} \text{3-1}$$

$$z = r(1 - \cos\theta) \hspace{3cm} \text{3-2}$$

where y and z are the horizontal and vertical coordinates respectively, $\theta \in [0, 2\pi]$ is the angle, in radians, of rotation of the circle defining the cycloid, and r is the radius of the generating circle (Wolfram Mathworld, 2014).

The ADINA model, as shown in Figure 8 and Figure 9, was defined using the same coordinate system established by Komendant.
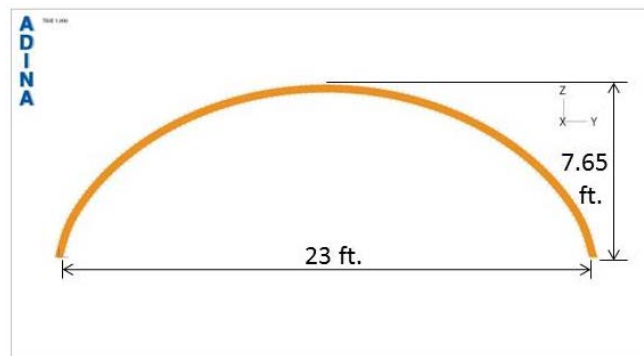
Figure 8. Cycloid model in the *y-z* coordinate plane (cross-section)
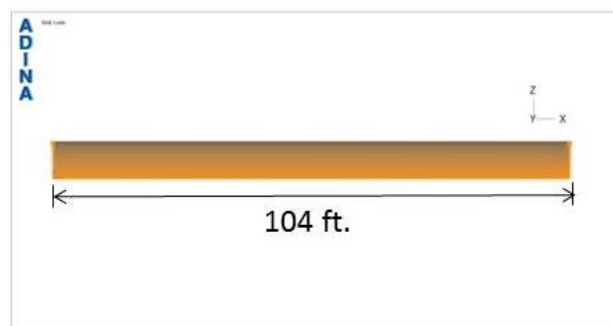
Figure 9. Cycloid model in the *x-z* coordinate plane (longitudinal elevation)

The thickness of the shell, t, is 4 inches according to the design documents (Komendant, 1970 p.2). Komendant introduces another variable, a_i, which he sets equal to four times the radius of the generating circle (Komendant, 1970 p 2). According to the design calculations, a_i has a value of 14.64 ft., which results in the generating circle radius of 3.66 ft. The span of the cycloid, B, corresponds to a full rotation of a generating circle and hence equals to the length of its circumference.

$$B = 2\pi r = 23\ ft \qquad\qquad 3\text{-}3$$

Komendant's calculations were based on the inside surface of the cycloid. In order to define the finite element model, the coordinates of the mid-surface of the cycloid were calculated. Due to the cycloid thickness of 4 inches, the mid-surface of the cycloid has a span of 23 ft and 4 inches. Thus, the radius of the generating circle for the mid-surface is 3.71 ft. The y and z coordinates of the mid-surface of the cycloid are presented in

The horizontal or y-coordinates on the mid-surface are equally spaced. Equations 3-1 and 3-2 were used to solve for the values of θ and z, given the y-coordinates and the radius.

When generating the coordinates of the inside and outside surfaces of the cycloid, the uniform thickness of 4 inches needs to be preserved. Thus, Equations 3-1 and 3-2 were differentiated in terms of θ, resulting in Equations 3-**4** and 3-**5**, and were applied to the cross-sectional geometry of the cycloidal shell shown in Figure 10.

$$\frac{dy}{d\theta} = r(1 - \cos\theta)$$

<div align="right">3-4</div>

$$\frac{dz}{d\theta} = r(\sin\theta)$$

<div align="right">3-5</div>

Table 2. Fifty _y_ and _z_ coordinates of the mid-surface of the cycloid

Y-coordinate (in)	Z-coordinate (in)	Y-coordinate (in)	Z-coordinates (in)
0.000	0.000	11.905	7.425
0.476	1.492	12.381	7.410
0.952	2.305	12.857	7.379
1.429	2.948	13.333	7.333
1.905	3.492	13.810	7.272
2.381	3.966	14.286	7.194
2.857	4.386	14.762	7.100
3.333	4.762	15.238	6.989
3.810	5.100	15.714	6.861
4.286	5.406	16.191	6.716
4.762	5.684	16.667	6.551
5.238	5.935	17.143	6.367
5.714	6.162	17.619	6.162
6.191	6.367	18.095	5.935
6.667	6.551	18.571	5.684
7.143	6.716	19.048	5.406
7.619	6.861	19.524	5.100
8.095	6.989	20.000	4.762
8.571	7.100	20.476	4.386
9.048	7.194	20.952	3.966
9.524	7.272	21.429	3.492
10.000	7.333	21.905	2.948
10.476	7.379	22.381	2.305
10.952	7.410	22.857	1.492
11.429	7.425	23.333	0.000
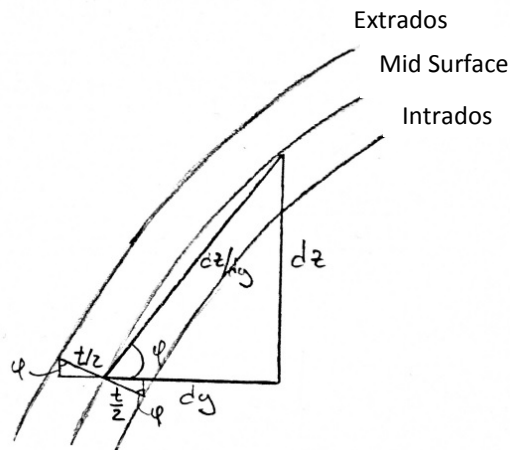
Figure 10. Drawing of the cross-section of the cycloidal shell.

The ratios of dz to dy for all values of ϕ (angle of the slope $\frac{dz}{dy}$ shown in Figure 10 and expressed in Equation 3-**7**) were then calculated using Equation 3-6, which was found by combining Equation 3-4 and 3-5.

$$\frac{dz}{dy} = \frac{\sin\theta}{1 - \cos\theta} \qquad \text{3-6}$$

Thus, we were able to determine the angle ϕ, which was necessary to calculate the coordinates of the inside and the outside surfaces of the cycloid. In order to do that, Equations 3-8 through 3-11 were developed using the geometry of Figure 10.

$$\phi = \arctan\left(\frac{dz}{dy}\right) \qquad \text{3-7}$$

$$z_{out} = z_{mid} + \frac{t}{2}\cos(\phi) \qquad \text{3-8}$$

$$y_{out} = y_{mid} - \frac{t}{2}\sin(\phi)$$

<div align="right">3-9</div>

$$z_{in} = z_{mid} - \frac{t}{2}\cos(\phi)$$

<div align="right">3-10</div>

$$y_{in} = y_{mid} + \frac{t}{2}\sin(\phi)$$

<div align="right">3-11</div>

The calculated points of the three surfaces are plotted in Figure 11.
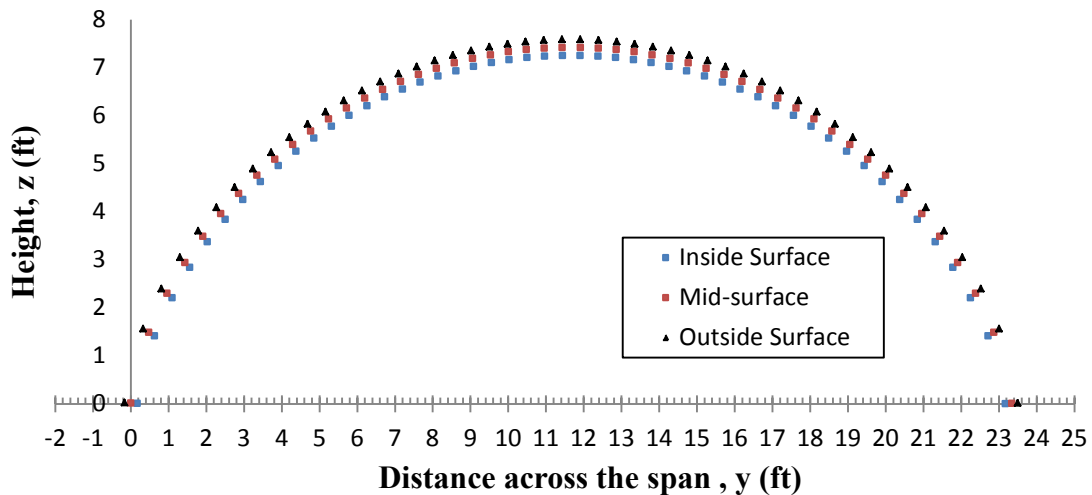
Figure 11. Inside, mid- and outside surfaces of a cycloid of Kimbell Art Museum

Based on Komendant's design, the total length of a representative cycloid, the edge and

the ring beams is 104 ft as mentioned in Chapter 1. The widths of the ring beams are 2 ft.

on each side, which results in an unsupported length of the cycloid of 100 ft.

(Komendant, 1970 p. 37). This unsupported length was used for all models except for

FEM-3 and FEM-6, which were fully supported along the edge. FEM-1 through FEM-7

did not include ring beams but still had to comply with the total length of 104 ft to allow

for fair comparison between models, and therefore the cycloids in those models were made 104 ft long.

The *y* and *z* coordinates defining the intrados and extrados were imported into ADINA and the points were then connected with the built-in spline polynomial function. The resultant cross-section of the cycloid was defined as a 2D surface in the *y-z* plane and then extruded 100 ft (1200 in.) or 104 ft (1248 in.) depending on the model along the positive *x*-axis to create a 3D solid volume.

3.2 Ring and edge beam geometry

The dimensions of the edge beam were obtained from the Komendant's design calculations (Komendant, 1970 p.1). Komendant provides dimensions for the entire beam that connects two cycloidal shells as shown in Figure 12.
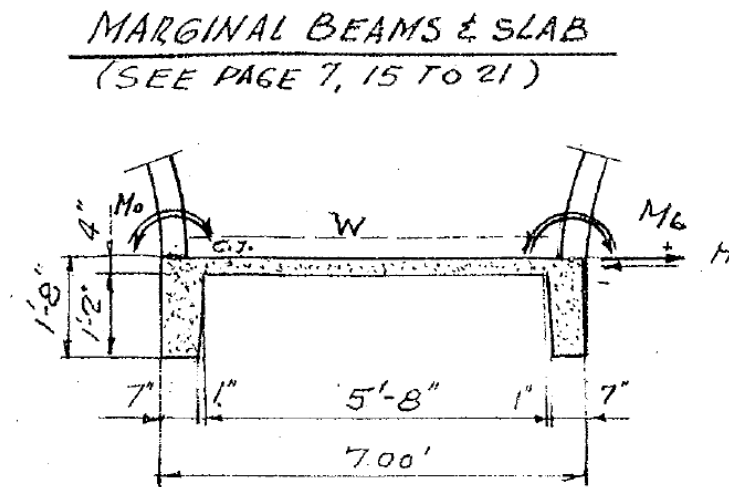
Figure 12. Drawing of a typical edge beam connecting two shells (Komendant, p. 24)

The coordinates for ADINA were generated manually by following the provided dimensions. The points were plotted in ADINA in the *y*- and *z*-axis and surfaces were created and extruded along the *x*-axis.

Komendant's calculations provide information about the varying thickness of the ring beams at every 10% in the *y*-direction along the intrados of the ring beam. A typical cross-section of the ring beam as well as its dimensions at the crown is given in Figure 13.
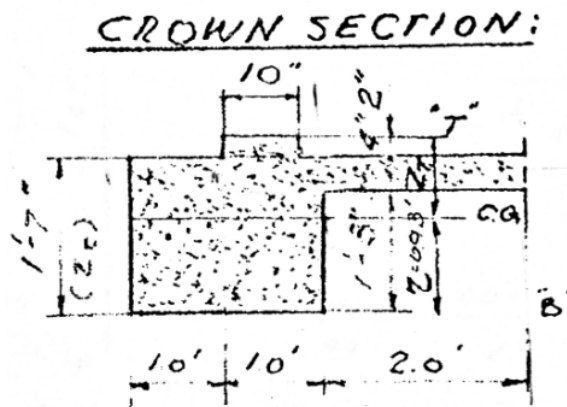
Figure 13. Cross-section of the ring beam at the crown (Komendant, 1970 p. 37)

The resultant values of the angle ϕ from Equation 3-7 were used in calculating the coordinates of the inside surface of the ring beam using Equation 3-12 and 3-13.

$$z_{in_{ring}} = z_{out} - t_{ring}\cos(\phi) \qquad \text{3-12}$$

$$y_{in_{ring}} = y_{out} + t_{ring}\sin(\phi) \qquad \text{3-13}$$

where t_{ring} is the thickness of the ring beam at every new increment along its circumference, y_{out} and z_{out} are the y and z coordinates of the outside surface of the cycloid and $y_{in_{ring}}$ and $z_{in_{ring}}$ are the y and z coordinates of the inside surface of the ring beam.

The coordinates defining the inside surface were plotted in ADINA in the *y-z* plane and were connected using the spline function as shown in Figure 15. The spline defining the extrados of the cycloid and the spline defining the intrados of the ring beam were connected with straight lines and thus a 2D surface in the *y-z* plane was created. The surface was extruded 2 ft. in the *x* direction. The same process was repeated on the other end of the cycloid and thus the second ring beam was defined. The calculated coordinates of the ring beam are shown in Figure 14.
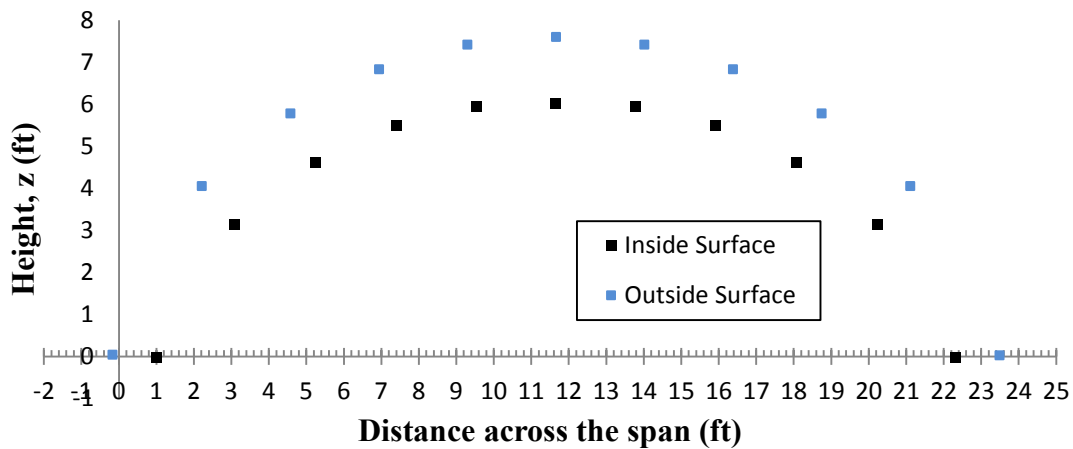
Figure 14. Plot of the intrados and extrados of the ring beam

The models of FEM-7 and FEM-8 that include ring beams can be found in Appendix A.

3.3 Prestressing cables: Geometry, Force and Meshing

The coordinates of the prestressing cables were based on data from Komendant's design calculations (Komendant, 1970, p.14). The coordinates of the prestressing cables were imported into ADINA and were connected using the built-in spline polynomial function as shown in Figure 15. Models FEM-2, FEM-5 and FEM-8 that include prestressing cables are shown in Appendix A.
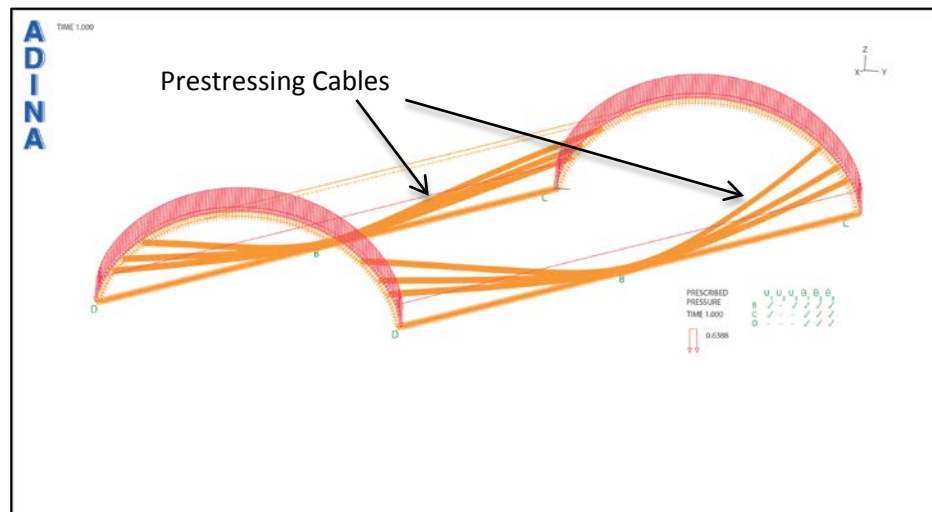
Figure 15. Prestressing cables in FEM-2.

The value of the prestressing force used in the ADINA models was determined by following Komendant's design calculations. Komendant uses six, 0.98 in^2 cables with an applied force of 174 kips per cable. This force corresponds to 75% of the ultimate allowable force per cable of 233 kips (Komendant, 1970 p.5). Komendant takes into account the impact of shrinkage and plastic flow on the loss of prestressing force.

Komendant calculates the stiffness of steel relative to the total stiffness, α, to be 0.0326

and the elastic modulus of the concrete, E_c to be approximately equal to 5,000,000 psi

(Komendant, 1970 p.6). He calculates the loss in prestressing force and determines that

the cables lose 111 kips of force in total, which results in a total force of 933 kips

(Komendant, 1970 p.6). Based on this information and the elastic modulus of steel of

29000 ksi, the strain in each prestressing cable, ϵ_{st}, was calculated as 0.0055 in/in.

$$\epsilon_{st} = \frac{933 \text{ kips}}{6 \text{ cables x } 0.98 \text{ in}^2 \text{ x } 29000 \text{ ksi}} = 0.0055 \text{ in/in} \qquad \text{3-14}$$

This strain of 0.0055 in/in was applied in the ADINA models to each cable as initial

strain. The cable lines were subdivided into 1 in. segments to allow for proper

smoothness of the truss elements as prescribed by ADINA. According to ADINA, the 3-

and 4-node truss elements should be employed in modeling cables and steel

reinforcement. Since the number of nodes is directly related to the solution accuracy, the

4-node truss elements were chosen to model the prestressing cables.

3.4 Material Properties

According to Specification for Reinforced and Prestressed Concrete for Kimbell

Art Museum, the strength of concrete used was prescribed to be 5000 psi (Komendant:

Specification 1970 p.6). Komendant uses the following equation to calculate the elastic

modulus of concrete (Komendant, 1970 p.6).

$$E_c = 8.15\text{x}10^6\text{x}\left(\frac{f'_c}{3300 + f'_c}\right) \approx 5\text{x}10^6 \text{ psi} \qquad \text{3-15}$$

However, based on the current Building Code Requirements for Structural Concrete (ACI 318-11) and Commentary the following equation should be used (American Concrete Institute, 2011).

$$E_c = 57000\sqrt{f}_c \approx 4\text{x}10^6 \text{ psi} \qquad\qquad 3\text{-}16$$

The value of the elastic modulus of approximately $5\text{x}10^6$ psi as calculated in Equation 3-15 was used in the ADINA models in order to facilitate comparison between the finite element output and Komendant's calculations. The elastic modulus of steel was defined as 29000 ksi by Komendant, and this value was used in the ADINA models (Komendant, 1970 p.6).

3.5 Elements and Meshing

In order to model the cycloids, both shell and 3D solid finite elements were considered. The benefit of using shell elements versus 3D solid element is that rotational degrees of freedom are defined for shell elements. This allows for automatic creation of moment diagrams and the evaluation of longitudinal and transverse moments in a structure. Therefore, initial models of the cycloid were made using shell elements. However, prestressing had to be included in FEM-7 and FEM-8. As mentioned earlier, the 3- and 4-node truss elements should be employed in modeling cables and steel reinforcement. The truss elements are compatible with shell elements; however rigid links between the truss elements and the shell elements have to be generated manually (ADINA, 2011). Due to the irregular three-dimensoinal geometry of the prestressing

cables it was decided to use the auto connect feature of ADINA, only available with 3D solids Thus, 3D solid elements were considered to model the cycloid. For every prestressing cable, the ADINA determined the intersections between the prestressing cable and the 3D solid elements (ADINA, 2011). Nodes were created at these intersections and truss elements were generated between the nodes (ADINA, 2011). ADINA then defined constraint equations between every generated node on the cable and the three closest corner nodes of the 3D solid element (ADINA, 2011).

The shell thickness of 4 in. is very small compared to its length of 100 ft. Due to such small ratio of thickness to length, according to ADINA, the use of 3D solid elements can result in a model that is too stiff with a poorly conditioned stiffness matrix (ADINA, 2011). Therefore, it was important to conduct an accuracy study to understand how many elements are required through the shell thickness. The study was conducted on a cycloid made up of 3D solid elements and supported on 4 surfaces as it will be shown in Chapter 3.7. Two surfaces on one end of the cycloid had all translational degrees of freedom fixed while the remaining surfaces were free to move along the *x*-axis only. The following nominal element dimensions in inches were considered: 4"x4"x12", 2"x2"x6" and 1"x1"x3". The first number corresponds to thickness, followed by width and length. As a result, 1, 2 and 4 elements through the thickness respectively were tested. The number of nodes in the 3D solid elements also varied as follows: 8, 10, 11, 20 and 27 nodes. The layout of nodes of the elements is presented in Figure 16.

(a) 20-, 21- & 27-node elements

(b) 8-node elements

(c) 4-, 10- and 11-node tetrahedral elements
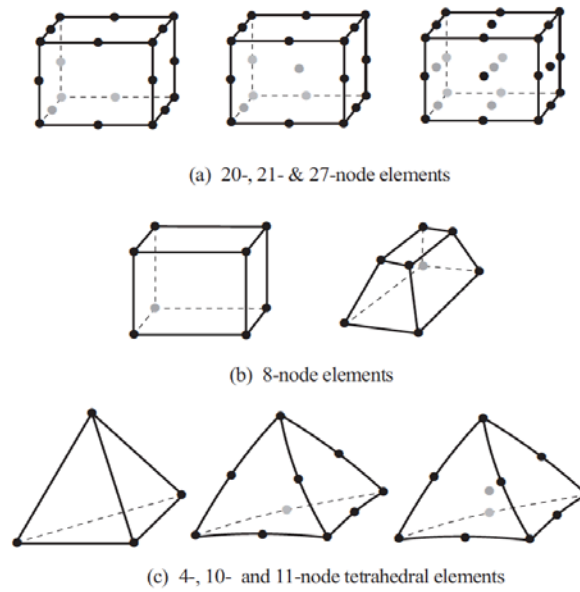
Figure 16. Node layout of 3D solid elements used in the study (ADINA, 2011).

The maximum deflections at the edge of the midspan of the cycloid are recorded in Table 3.

Table 3. Maximum vertical deflections of the 3D solid cycloid for various mesh sizes

Vertical deflection at the edge of mid-span (in.)					
Mesh size	8 Nodes	10 Nodes	11 Nodes	20 Nodes	27 Nodes
4x4x12	-3.186	-3.347	-3.348	-3.318	-3.302
2x2x6	-3.346	-	-	-3.401	-
1x1x3	-3.405	-	-	-3.442	-

A similar study was conducted with the cycloid made up of shell elements and supported at 4 corners. Two corners on one end of the cycloid had all translational degrees of freedom fixed while the remaining corners were free to move along the *x*-axis only. The

nominal element size of 4x4x12 was used with 8 nodes per element. To allow for fair comparison, the rotation around all three axes was released for the shell model, since in addition to the translational degrees of freedom shell elements also possess rotational degrees of freedom. The maximum deflection of the cycloid at the edge of the midspan was determined to be 3.361 in. However, it is important to note that the loading in the shell model is applied to the midsurface of the shell, which is different than the 3D solid element model, where the loading is applied to the extrados surface. The support reactions were determined for the shell model and the 3D solid model based on the ADINA analysis output files. The shell model had a total reaction of 302,765 lb. and the 3D solid model had a total reaction of 308,206 lb., which results in an increase of 1.8%. Thus, the deflection of 3.361 in. was scaled up by 1.8%, resulting in a deflection of 3.421 in. This was taken as a reference deflection value, to which the 3D solid model deflections were compared. The 3D solid model with 1x3x3 meshing and 20 nodes per element yielded one of the closest values of deflection with an error of 0.61%. Thus, the study showed that the use of sufficiently fine 3D solid elements eliminates the problem of artificially high stiffness. Therefore, 3D solid elements with a nominal size of 1x3x3 and 20 nodes per element were used in modeling the cycloid, the ring and the edge beams.

3.6 Loads

According to Komendant's design, normal weight concrete of 150 pcf was utilized, which results in 0.347 psi load on a 4 in. thick cycloidal shell (Komendant, 1970 p.2). Komendant also includes a 30 psf (0.208 psi) snow load and 12 psf (0.083 psi) from a 2

in. thickness of insulation (Komendant, 1970 p.3). All gravity loads were applied in the global z direction in the ADINA models as shown in Figure 17.
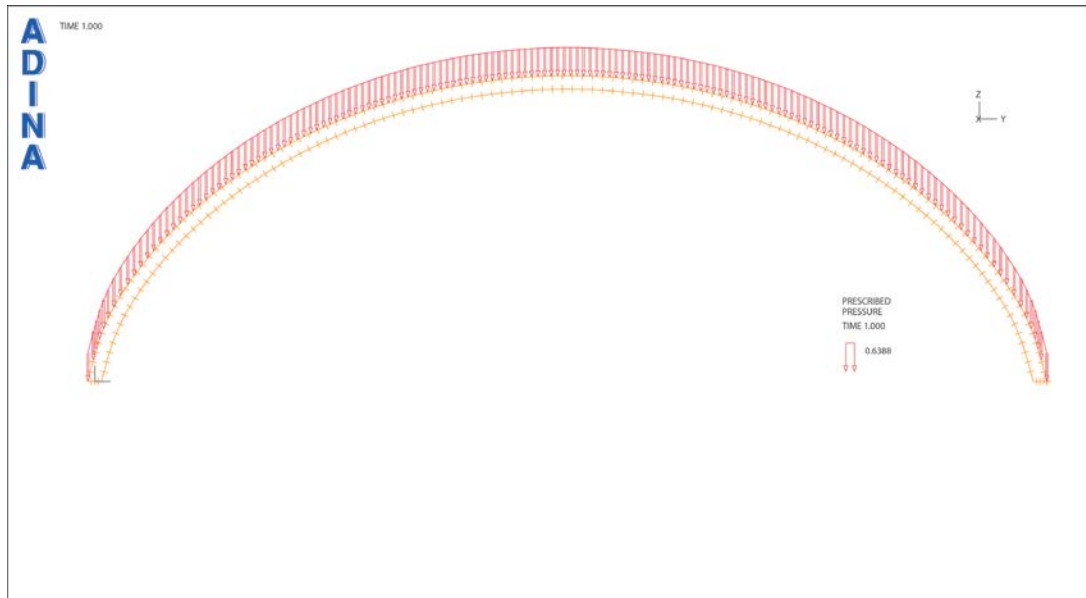
Figure 17. Loading pattern of the gravity loads

Thus, the total distributed load on the cycloid is equal to 0.639 psi.

The edge beams have a cross-sectional area of 2 ft^2, which results in dead load of 25 lb/in (Komendant, 1970 p.29). Komendant includes an additional dead load of 40 psf due to the insulation, which results in 10-lb/in acting on half of the edge beam shown in Figure 12. The projected width of the snow load for half of the edge beam was determined from Figure 12 to be 2.67 ft. The resultant snow load was calculated to be 8.34 lb/in along the length of the edge beam. Thus, the total load on the edge beam is equal to 43.34 lb/in. The distributed load was applied along the edge of the beam as shown in Figure 18.
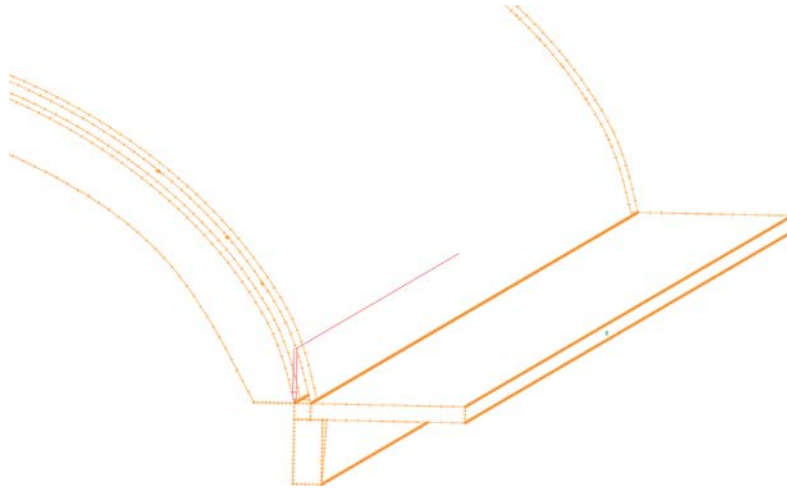
Figure 18. Distributed load (red) applied along the length of the edge beam

3.7 Supports and Boundary conditions

The shells of Kimbell Art Museum are supported by columns that are 2 ft by 2 ft in cross-section. Therefore, all models except for FEM-3 and FEM-6, were supported by four surfaces, each having the dimensions of 4 in. by 24 in as shown in Figure 19.

Figure 19. Typical support surface for FEM-1, 2, 7 and 8.

The surfaces had to be meshed differently than the rest of the structure for ADINA to recognize them as part of the assembly. The decision about the element type to be used for the surfaces was made between plate and shell elements. Two-dimensional 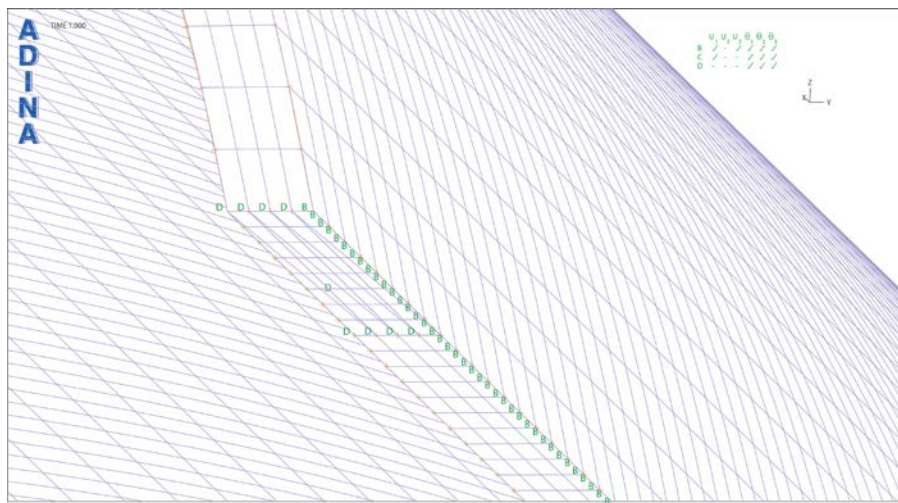solid elements were not found to be suitable because, according to ADINA, they have to be located in the y-z plane, while the support conditions are located in the x-y plane. No apparent differences between shell and plate elements relevant to the intents of the study were found. Plate elements were chosen because they exist in a single 3-node configuration. The thickness of plate elements was chosen to be 0.1 in. because it is too small to alter the geometry in the cycloid but large enough to avoid computational problems.

The movement of the edge lines was restrained along the y-axis in order to model the symmetry. More sophisticated models, such as FEM-7 and 8, had to be supported at multiple locations on every corner. For example, in the model with the ring and edge beams, the ring beam had to be supported at the springing due to an overhang as shown in Figure 22 and the edge beam had to be supported at its corners directly below the ring beam as shown in Figure 23. All models with their support conditions are presented in Appendix A. Pin supports had all translational degrees of freedom (DOFs) fixed and all rotational degrees of freedom free. Roller supports had all translational DOFs fixed except for translation along the x-axis. Rotational DOFs for the roller were prescribed as free. Since the models represent a portion of the roof system, a symmetry boundary condition was applied to all models. The edges or beams in the models were allowed to

move along the x- and z-axes, however the movement along the y-axis was fixed. All rotational degrees of freedom were fixed except for rotation around the y-axis.

Chapter 4: Analysis Results

4.1 Review of Komendant's calculations

The review of Komendant's calculations revealed several key values, which are summarized in Table 4. The notation used to describe the values as well as references to Komendant's calculations are described as follows. The vertical deflection at the midspan due to loads is denoted as $\delta_{loads,}$ (Komendant 1970, p. 7), the deflection at the midspan due to the prestressing force at $t = 0$ or $t = n$ is denoted as $\delta_{PT\ t=0}$ (Komendant 1970, p. 7) and $\delta_{PT\ t=n,}$ respectively (Komendant 1970, p. 8). The vertical deflection at the midspan due to a combined effect of loads and the prestressing force at $t = 0$ or $t = n$ is denoted as $\delta_{loads\ and\ PT\ t=0}$ (Komendant 1970, p. 7) and $\delta_{loads\ and\ PT\ t=n}$ (Komendant 1970, p. 8), respectively. The maximum longitudinal moment at the midspan is denoted as M_{y-y}, while the reaction per support is denoted as $R_{support}$ (Komendant 1970, p. 4). The longitudinal stress at the crown and the edge of the mid-span cross-section without prestressing is denoted as $\sigma_{top\ no\ PT\ x-x}$ (Komendant 1970, p. 4) and $\sigma_{bot\ no\ PT\ x-x}$ (Komendant 1970, p. 4) respectively. The longitudinal stress at the crown and the edge of the mid-span cross-section with prestressing at $t = 0$ or $t = n$ is denoted as $\sigma_{top\ with\ PT\ x-x\ t\ =\ 0}$ (Komendant 1970, p. 5) and $\sigma_{bot\ with\ PT\ x-x\ t\ =\ 0}$ (Komendant 1970, p. 5) as well as $\sigma_{top\ with\ PT\ x-x\ t\ =\ n}$ (Komendant 1970, p. 6) and $\sigma_{bot\ with\ PT\ x-x\ t\ =\ n}$ (Komendant 1970, p. 6). Finally, the transverse moment at the crown of the mid-span cross-section with and without the use of prestressing is denoted as $M_{transverse\ at\ crown}$ and $M_{transverse\ at\ crown\ with\ PT}$, respectively (Komendant 1970, p. 17). These values represent the final results of all Komendant's

calculations that were compared with the FEA models that were made. Komendant's results from irregular wind distribution, short shells, column and other analyses were not considered. The Kimbell Art Museum includes several shells of shorter length, in addition to the standard 100 ft. long cycloids, which Komendant analyzes. However Komendant is primarily concerned with the cross-section at the mid-span of the 100 ft. long cycloid being studied. Figure 20 shows the location of the cross-section under consideration.

Table 4. Key values from the Kimbell Art Museum design calculations

δ_{loads} (in)	-0.5904	$\sigma_{bot\ no\ PT\ x\text{-}x}$ (psi)	1242
$\delta_{PT\ t=0}$ (in)	0.438	$\sigma_{top\ with\ PT\ x\text{-}x\ t=0}$ (psi)	-891
$\delta_{PT\ t=n}$ (in)	0.209	$\sigma_{bot\ with\ PT\ x\text{-}x\ t=0}$ (psi)	-51
$\delta_{loads\ and\ PT\ t=0}$ (in)	-0.152	$\sigma_{top\ with\ PT\ x\text{-}x\ t=n}$ (psi)	-903
$\delta_{loads\ and\ PT\ t=n}$ (in)	-0.3814	$\sigma_{bot\ with\ PT\ x\text{-}x\ t=n}$ (psi)	37
$M_{y\text{-}y}$ (k-ft)	4700	$M_{transverse\ at\ crown}$ (kip-ft)	-0.125
$R_{support}$ (kip)	90.5	$M_{transverse\ at\ crown\ with\ PT}$ (kip-ft)	0.105
$\sigma_{top\ no\ PT\ x\text{-}x}$ (psi)	-1067		

Komendant analyzes the cycloid as a beam in the long direction. The validity of this design assumption will be evaluated using the finite element models that were created in ADINA. Due to this approach, Komendant gives a single value of vertical deflection for each loading case, which could have been considered as the maximum

value. In his calculations, Komendant calculated the deflection due to the full dead and live load, which was determined to be -0.5904 in. (Komendant 1970, p. 7). A negative sign stands for downwards deflection in the negative z direction, while a positive sign corresponds to uplift in the positive z direction. He then included the effect of prestressing and calculated two values: one at $t = 0$ and the other at $t = n$ in order to consider creep, shrinkage and loss of the prestressing force. The upward deflection caused by the prestressing cables was calculated to be 0.439 in. and 0.209 in. for $t = 0$ and $t = n$, respectively (Komendant 1970, p. 7-8). Thus, the total deflection that Komendant expected to see in his structure was calculated to be -0.152 in. and -0.3814 in. for $t = 0$ and $t = n$ respectively (Komendant 1970, p. 7; Komendant 1970, p. 8).

Komendant calculated the value of maximum moment about the longitudinal, y-axis to be 4700 k-ft. and the value of reaction per support to be 90.5 kips (Komendant 1970, p. 4). Komendant calculates the longitudinal and radial stresses in the cross-section shown in Figure 20. The negative sign stands for compression, while positive sign corresponds to tension. The longitudinal stress due to dead and live loads was calculated to be -1067 psi in compression at the crown and 1242 psi in tension at the bottom of the edge beam (Komendant 1970, p. 4). With the addition of prestressing at $t = 0$, the total longitudinal stress at the crown changes to -891 psi in compression and the longitudinal stress at the bottom of the edge beam changes to -51 psi in compression (Komendant 1970, p. 5). At $t = n,$ the stress at the crown increases to -903 psi in compression and tension stress of 37 psi develops at the bottom of the edge beam, which Komendant considers acceptable (Komendant 1970, p. 6). Considering the strength of concrete of

5000 psi, the compressive stresses correspond to less than 20% of that value. The tension

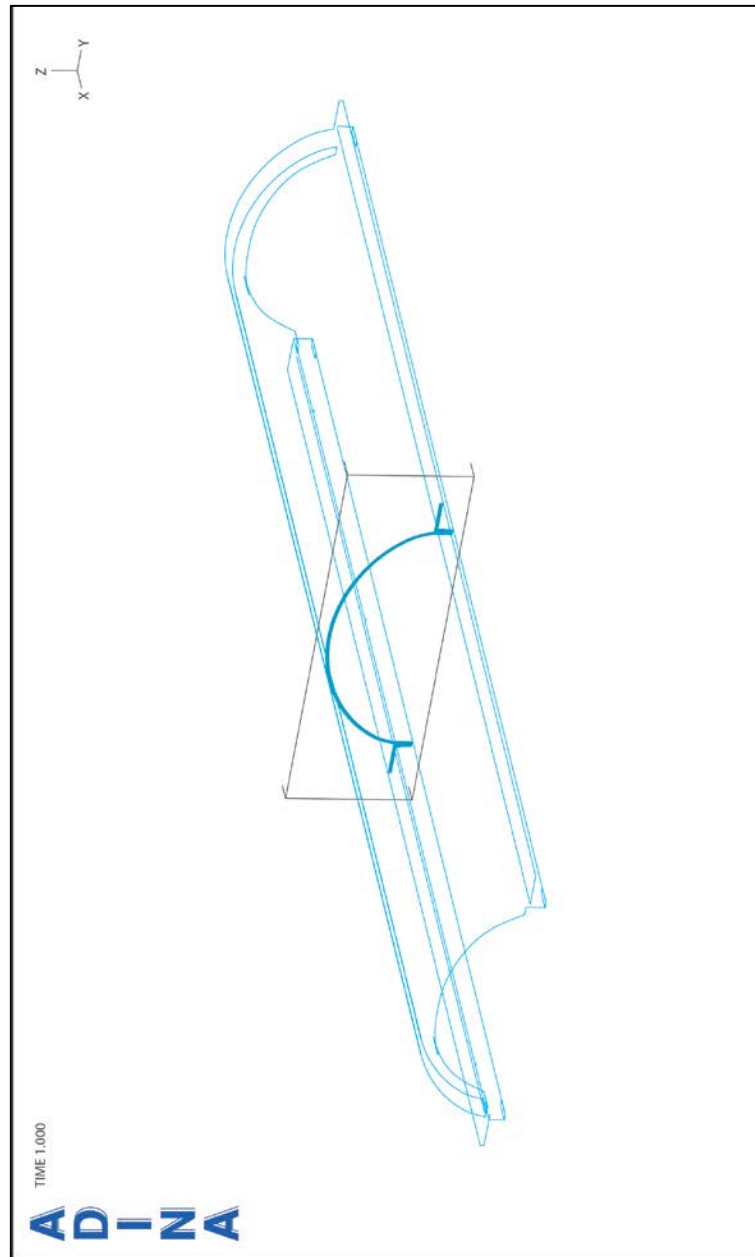stress that is developed is negligible and is counteracted by the steel reinforcement.

Figure 20. Cross-Section of the cycloidal shell being studied

For the transverse behavior, Komendant analyses the cycloid as an arch. Komendant states that the transverse moment due to dead and live loads is not a function of the length of the cycloid, however the moments due to prestressing vary along the length of the shell (Komendant 1970, p. 17). While stating that he acknowledges the variation in moment distribution, in his calculations he only presents the moment diagram for the cross-section shown in Figure 21. The values for the transverse moments listed in Table 4 were taken at the crown of the cycloid shown in Figure 21.
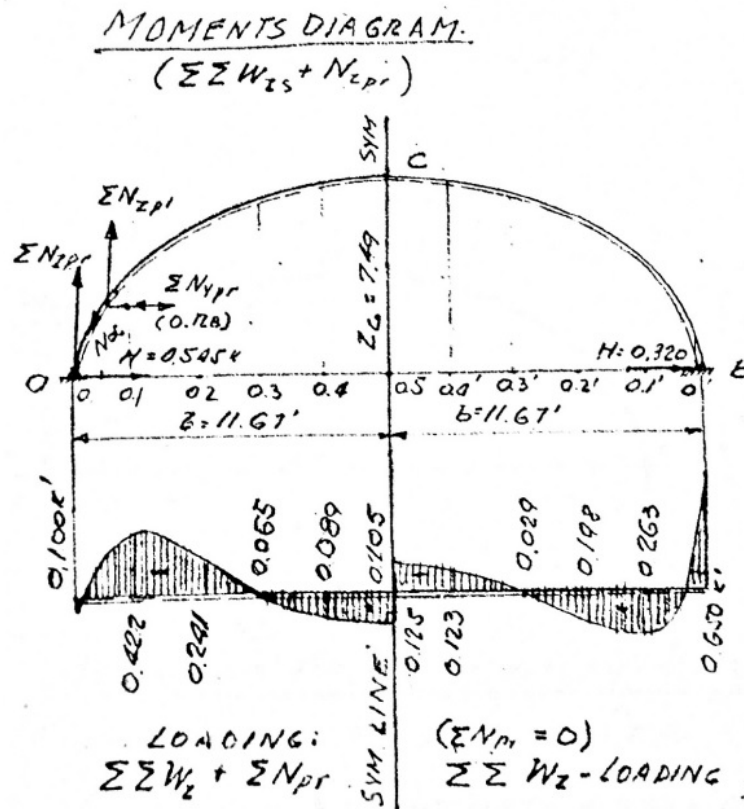

Figure 21. Transversal moment diagrams for the midspan of the shell (Komendant 1970, p. 17).

The diagram on the right half presents the transverse moments created by the dead and live loads, while the diagram on the left takes into account the addition of the prestressing force and the resultant additional transverse moment. The transverse moments presented in Table 4 were converted into stress in order to compare to FEM-8. It was assumed that the moment would act on a cross-section of 4" by 12" and no axial component would be present. As a result, -0.125 k-ft corresponds to 46.9 psi in tension at the top and -46.9 psi of compression at the bottom of the crown and 0.105 k-ft corresponds to 39.4 psi in tension at the bottom and -39.4 psi of compression at the top of the crown.

4.2 Development of Finite Element Models

FEM-1 was the simplest model that was created. The model had pressure applied to it in the global z direction as described in Chapter 3.6, however the distributed line loads were not present, since the edge beams were not used in this model. The implications of the difference in loading conditions are such that FEM-1 cannot be directly compared to Komendant's calculations, which include edge and ring beams.

FEM-2 explored the possibility of preserving the geometry and boundary conditions of FEM-1, but improving the performance of the shell via the use of prestressing. The support conditions, meshing size and the choice of element type remained the same with an addition of truss elements to represent prestressing cables in the manner described in the earlier chapter.

The purpose of FEM-3 was to simulate the possibility of constructing the shell on top of two rigid walls and thus forcing the shell to behave as a series of arches. All loads

are carried in the transverse direction only. The shell's geometry and the choice of element type remained the same as in FEM-1. The displacements on both edges were restrained in the direction of x-, y- and z-axes.

The purpose of FEM-4 was to simulate the possibility of stiffening the shell by rigid end walls. As mentioned in Chapter 1, the stiffening options used in FEM-3 and FEM-4 were very common in the days of early shell design because mathematically they created boundary conditions, which were very simple to solve. The symmetry boundary condition remained the same as in FEM-1; however, the displacements of the ring surfaces were restrained in the direction of x-, y- and z-axes. Symmetry constraint was imposed along the edges restraining displacements in the direction of y-axis. The shell's geometry and the choice of element type remained the same as in FEM-1.

FEM-5 explored the combined effect of supported ring surfaces and using prestressing. The support conditions, meshing size and the choice of element type remained the same as in FEM-4 with an addition of truss elements.

FEM-6 analyzes the combined effect that the fully supported edge and end ring surfaces have on the shell. FEM-6 serves as an extreme case of stiffening the shell that a designer can achieve. The meshing size and the choice of element type stays the same as in either FEM-4 of FEM-5, however the support conditions are a combination of support conditions of FEM-4 and FEM-5.

FEM-7 models the ring and edge beams that Komendant used in the design of Kimbell Art Museum. The choice of element type as well as meshing for the cycloid

remained the same as in FEM-1. The ring beams were also meshed with 20 node 3D solid elements that had nominal dimensions of 1"x3"x3" as shown in Figure 22. Automatic meshing was done by ADINA while keeping the 1"x3"x3" parameter, so there is a certain variation in element size and geometry.
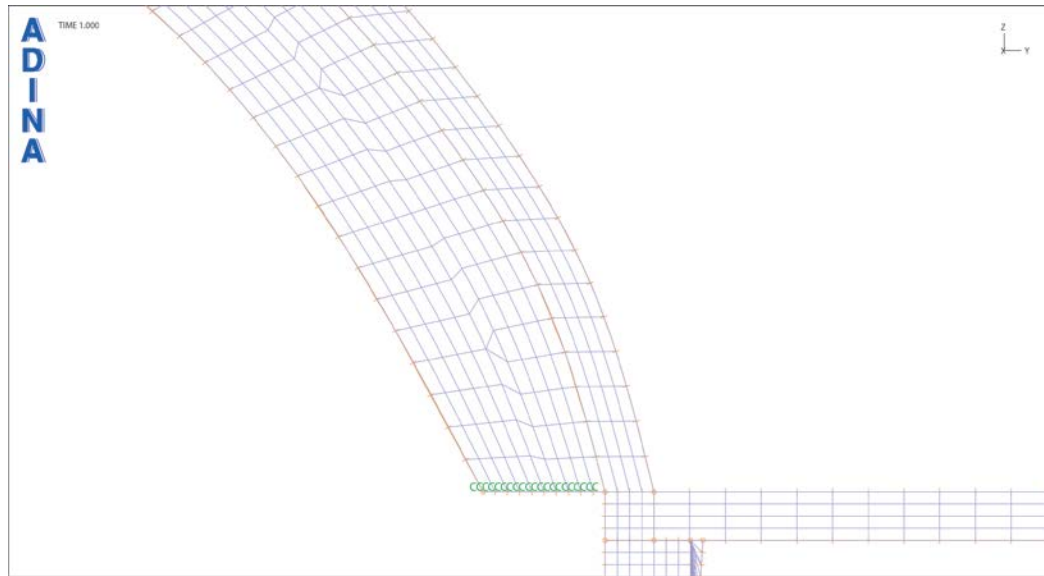

Figure 22. Meshing of the ring beam used for FEM-7 and FEM-8.

The edge beam surfaces' subdivisions were interrelated and therefore not all elements have dimensions of 1"x3"x3", however a common 1:3 ratio was preserved. Figure 23 contains an enlarged cross-section of one of the two edge beams with meshing and surface numbers.
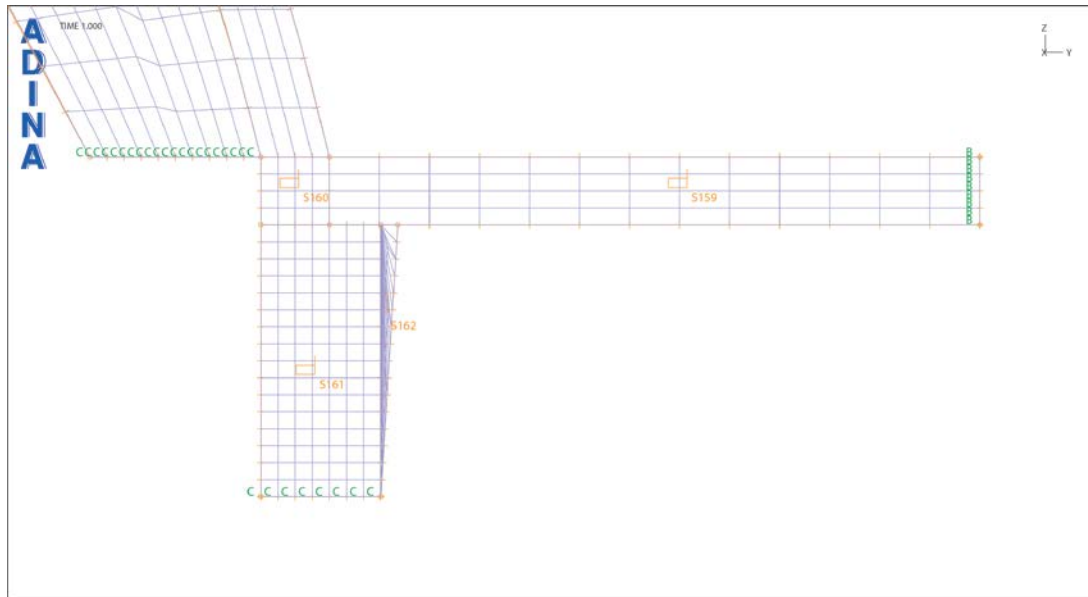
Figure 23. Meshing of the edge beam used for FEM-7 and FEM-8.

The support conditions of FEM-7 were the same as FEM-1 but applied to the edge and ring beams.

Finally, FEM-8 presents the most realistic model, which utilizes physical edge and ring beams together with prestressing. The geometry, meshing and support conditions remain the same as in FEM-7 with an addition of prestressing cables. This model will be compared with Komendant's calculations and contrasted with the preceding FEM models.

Chapter 5: Results and Discussion

Linear elastic analysis was performed on all of the models. Key numerical results from the cross-section under consideration are compiled in Table 5. The following information was collected: deflection at the crown and the edge, denoted as δ_{top} and δ_{bot} respectively; longitudinal stress at the crown and the edge, denoted as $\sigma_{top\ xx}$ and $\sigma_{bot\ xx}$; and finally radial stress at the top, mid- and bottom surface of the crown denoted as $\sigma_{top\ yy}$, $\sigma_{mid\ yy}$ and $\sigma_{bot\ yy}$ respectively.

Table 5. Data collected from the FEM models

	FEM-1	FEM-2	FEM-3	FEM-4	FEM-5	FEM-6	FEM-7	FEM-8
δ_{top} midspan (in)	-1.284	-0.1058	-0.0258	-0.3285	-0.0949	-0.0265	-0.4681	-0.1739
δ_{bot} midspan (in)	-1.328	-0.104	0	-0.3669	-0.0119	0	-0.5044	-0.1485
$\sigma_{top\ xx}$ (psi)	-1141	-372.4	-26.1	-442.4	-163.5	-39.5	-742.4	-795.4
$\sigma_{bot\ xx}$ (psi)	2179	-1583	varies about 0	929.7	-946	varies about 0	996.4	-346.5
$\sigma_{top\ yy}$ (psi)	138.3	-240.2	-132.9	112.4	-292.4	-136.2	88.2	-125.5
$\sigma_{mid\ yy}$ (psi)	-9.47	-15.8	-20.9	-19.9	-13.51	-21.4	-37.4	-22.2
$\sigma_{bot\ yy}$ (psi)	-226.6	215.6	93.5	-194.5	274.8	97.5	-165.6	82.9

In order to be able to compare the FEM models to Komendant's calculation, data was collected at the same locations as described in Section 4.1 and summarized in Table 4. Since only one value of the initial prestressing strain was used, the change in deflection and stresses between $t = 0$ and $t = n$ was not taken into account. Also, the 3D solid elements do not possess rotational degrees of freedom, which doesn't allow an automatic creation of a moment diagram. Therefore, in order to investigate the moment at the crown of the cycloid, radial stresses were collected at the extrados, mid-surface and intrados locations and were compared to Komendant's moment values that were converted into values of bending stress.

Based on the analysis that was carried out, the deflection at the cross-section of interest is plotted in Figure 25. The deflected shape of FEM-1 is plotted in Figure 25. The deflected shape tells the direction of deflection, concavity of the structure, which helps visualize the distribution of compressive and tensile stresses in the structure. Based on this deflected shape, tensile stress is expected at the edge while compressive stress would develop at the crown. The analysis showed that the deflection at the cross-section of interest varies between -1.284 in. and -1.329 in. at the crown and edge respectively.
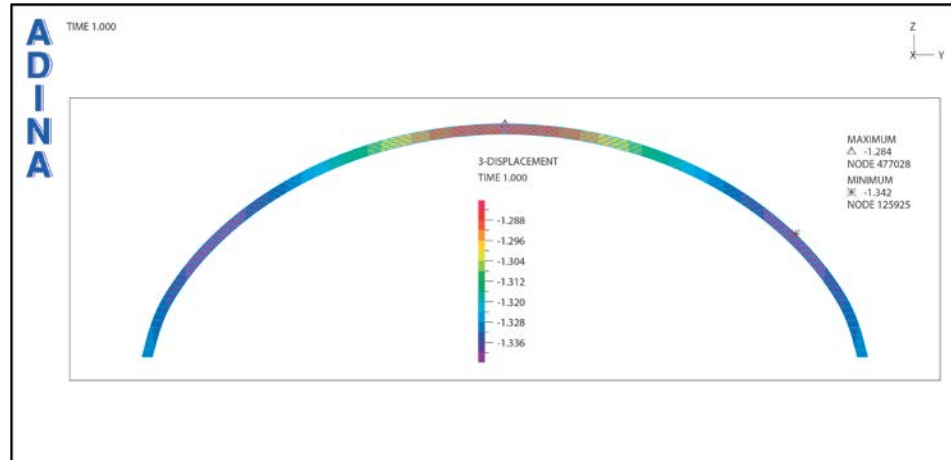
Figure 24. Plot of vertical deflection (in) at the midspan cross-section of FEM-1
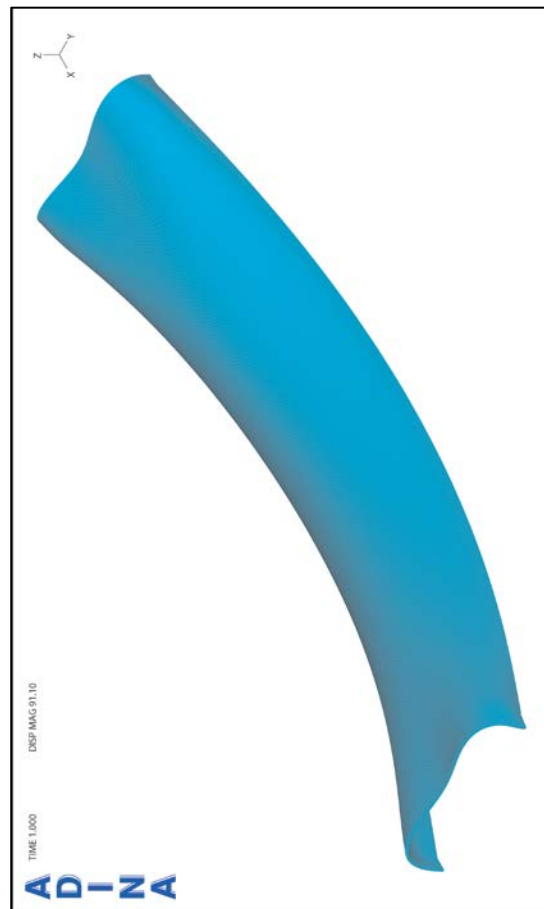

Figure 25. Deformed shape of FEM-1.

The values of deflection are significantly greater than the ones determined by Komendant. The absence of any stiffening and prestressing significantly increases the deflection. Without the rigid supports and prestressing the structure also develops significant tensile stress of 2250 psi in the longitudinal direction as shown in Figure 26. Such tensile stress is not acceptable because it would require heavy reinforcement, which is impractical in a 4" thick shell.
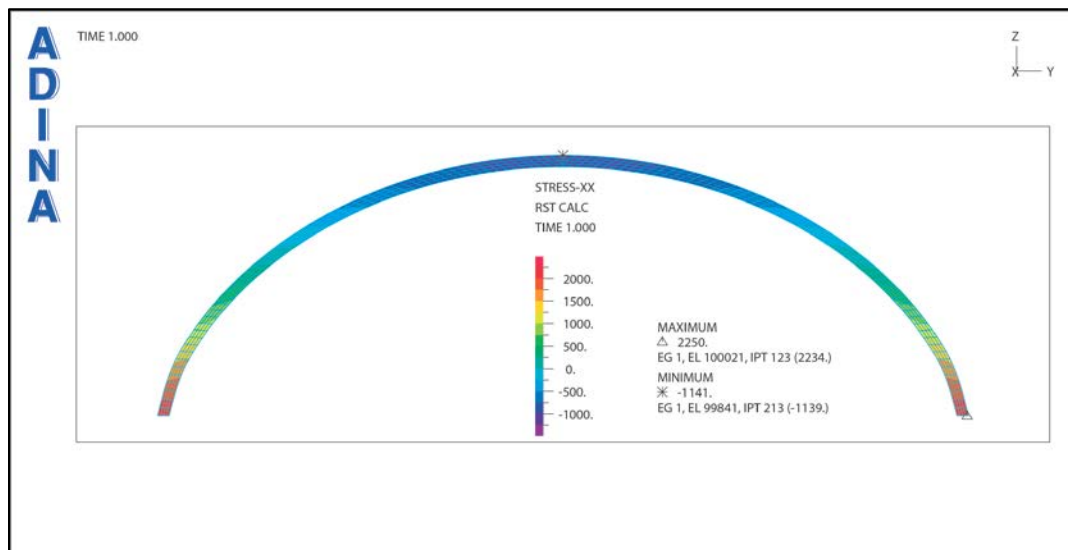
Figure 26. Longitudinal stresses (psi) at the mid-span cross-section of FEM-1

In the radial direction, the cycloid develops a significant amount of stress as shown in Figure 27.
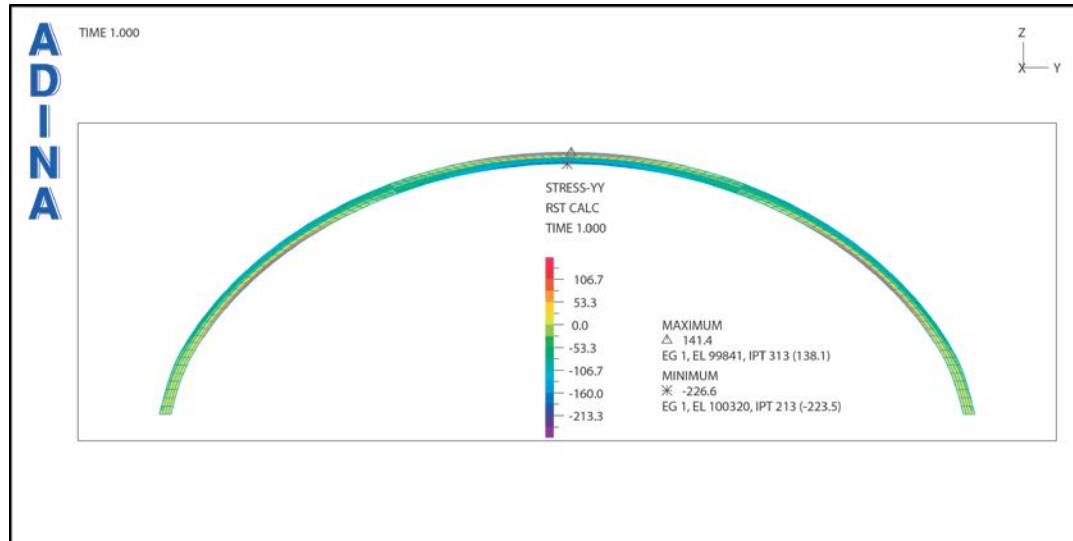
Figure 27. Radial stresses (psi) at the mid-span cross-section of model FEM-1

The stress at the midsurface of the cycloid's crown was found to be -9.47 psi. This stress is important in evaluating the transverse moment at the crown because it indicates the presence of the axial stress acting uniformly over the crown's cross-section. The deflected shape of the cycloid supported at four corners shows that the structure exhibits beam-like behavior. The above statement is supported by the plot of longitudinal stresses along the entire length of the shell created on the deformed shape of FEM-1 in Figure 28. Even though tensile and compressive stresses are not uniform along the length of the cycloid, the plot shows that stresses are distributed along the length of the shell as they would be in a beam.
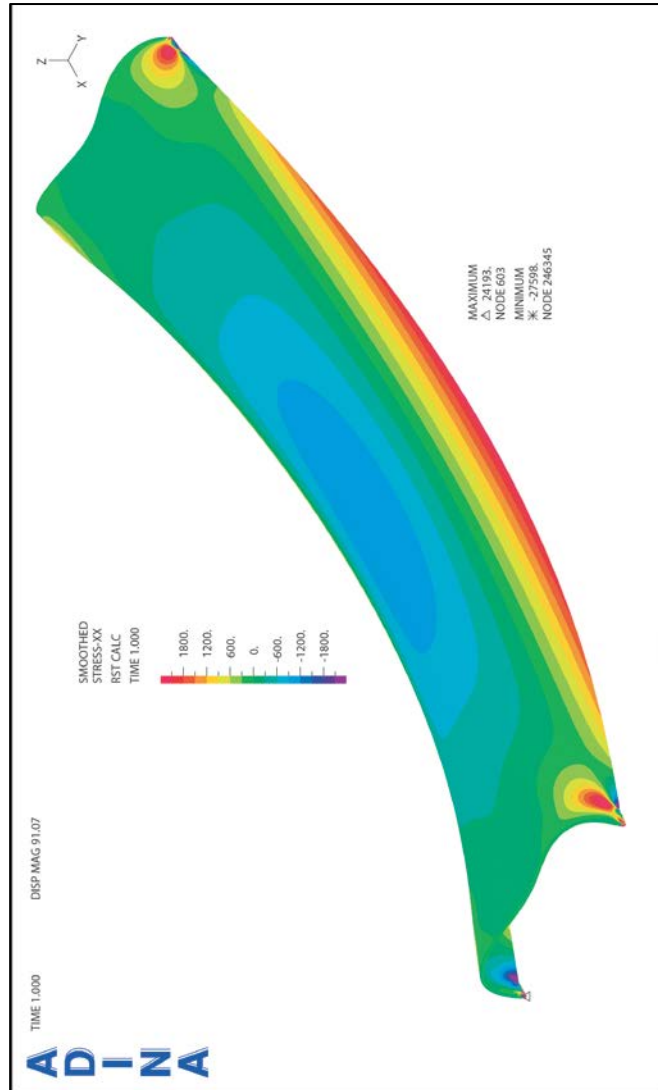
Figure 28. Longitudinal stress on the deformed shape of FEM-1

Early German shell designers stiffened their shells by fully supporting the edge, framing them into a wall or doing both. These three boundary constraint options were studied using ADINA in FEM-3, FEM-4 and FEM-6 respectively. If the edge is fully supported as in FEM-3, the shell stops behaving like a beam and instead behaves like a series of arches. The above statement is supported by the plot of longitudinal stresses

along the length of the deformed shape of FEM-3 in Figure 29. The longitudinal stress develops at the edge, since the displacement is restrained along the *x*-axis. However, the longitudinal stress within the cycloid varies about zero, which implies that no stress is distributed longitudinally and thus FEM-3 exhibits arch-like behavior.
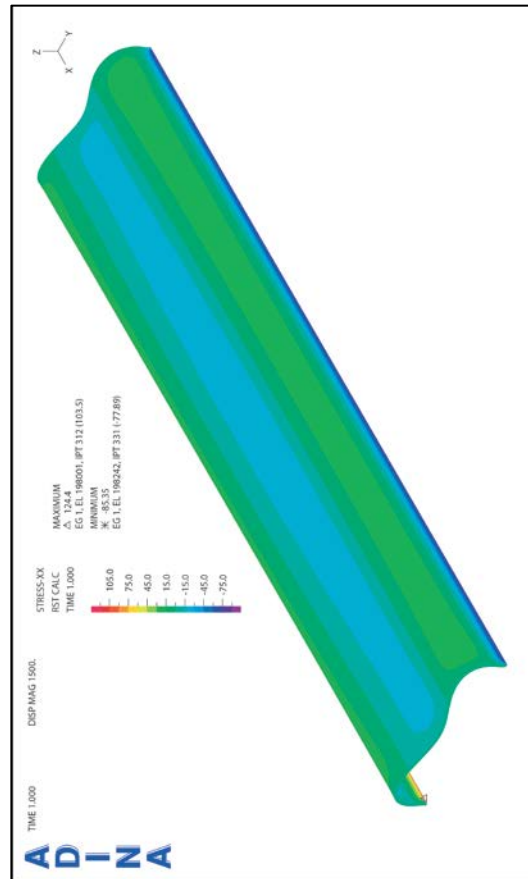

Figure 29. Longitudinal stress on the deformed shape of FEM-3

The results of FEM-3 show the deflection at the crown of -0.0258 in. with longitudinal stress of -26.1 psi at the crown as shown in Figure 30 and Figure 31 respectively. At the edge of the studied cross-section, longitudinal stress varies about 0 psi because as the shell deforms it tries to bend inwards in the radial direction, but is restrained from

movement in that direction. As a result, the shell's edge develops tension on the inside and compression on the outside.
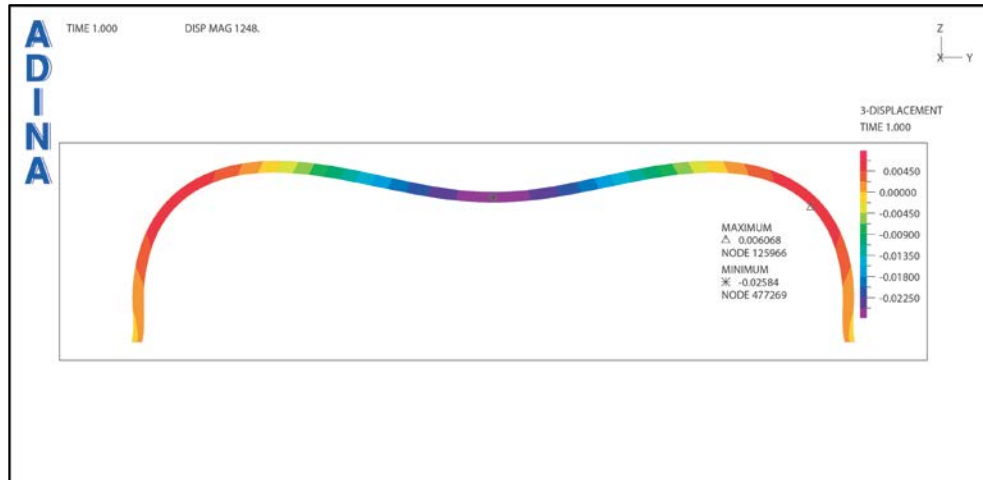

Figure 30. Plot of vertical deflection (in.) at the midspan cross-section of FEM-3
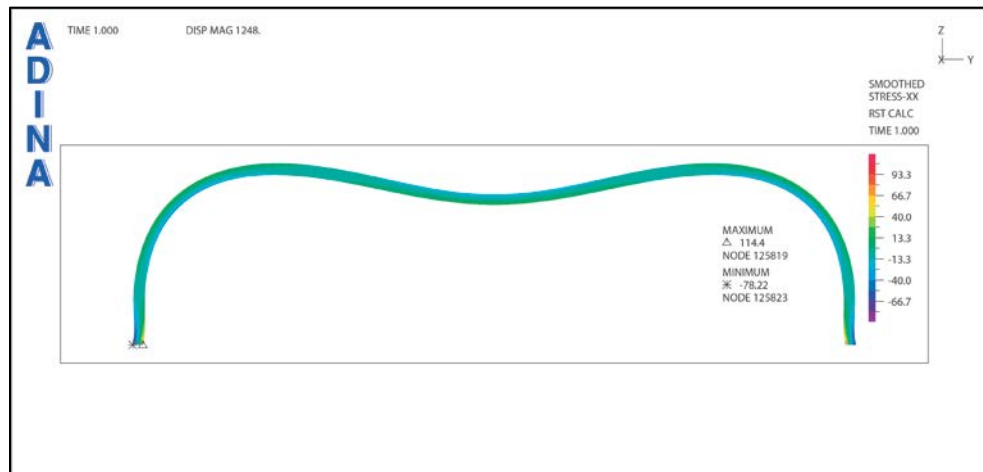

Figure 31. Longitudinal stresses (psi) at the mid-span cross-section of FEM-3

The stress at the crown of FEM-3 is opposite in sign compared to that of FEM-1, because the crown flattens out in FEM-3 as opposed to compressing in FEM-1. The deflected shape of FEM-3 results from the full support of the edge of the shell, forcing it

to behave as a series of arches. The radial stress decreased with a fully supported edge, most noticeably at the bottom of the crown, where -226.6 psi of compression (FEM-1) transformed into 93.5 psi in tension (FEM-3) as shown in Figure 32.
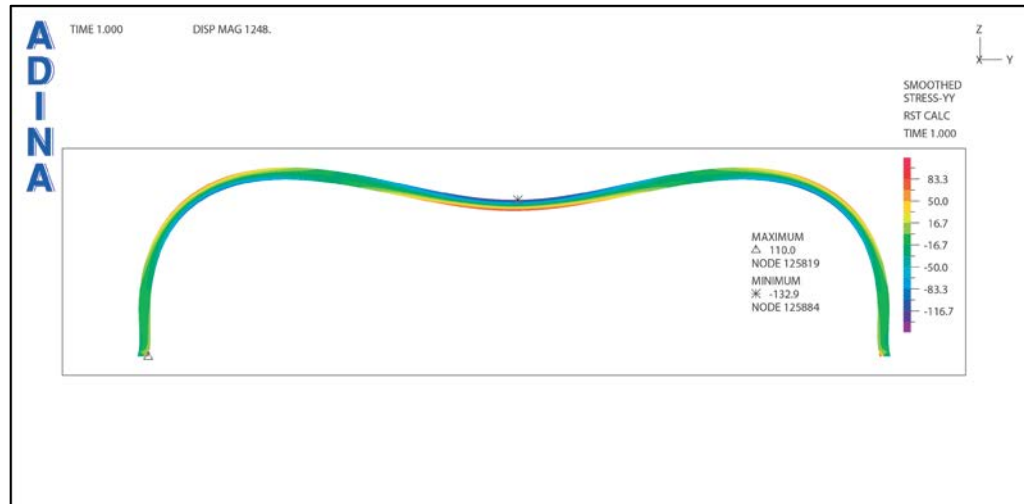

Figure 32. Radial stresses (psi) at the mid-span cross-section of FEM-3

While being a simple solution to the problem, FEM-3 is definitely not the most economical because material is not used in the most efficient manner possible. Fully supporting both the ring and the edge of the cycloid as shown in FEM-6, in fact, negatively impacts the performance as compared to FEM-3. The deflected shape of the entire shell exhibits arch-like behavior along the length of the shell except for the regions immediately outside the rings, where beam-like behavior takes place. As shown in Figure 33, approximately zero stress develops along the length of the shell, however more pronounced tensile and compressive longitudinal stresses develop at the rings, since concrete pulls away from the shell's crown and pushes against the edges. The latter is caused by the shell being restrained from movement along the x-axis.
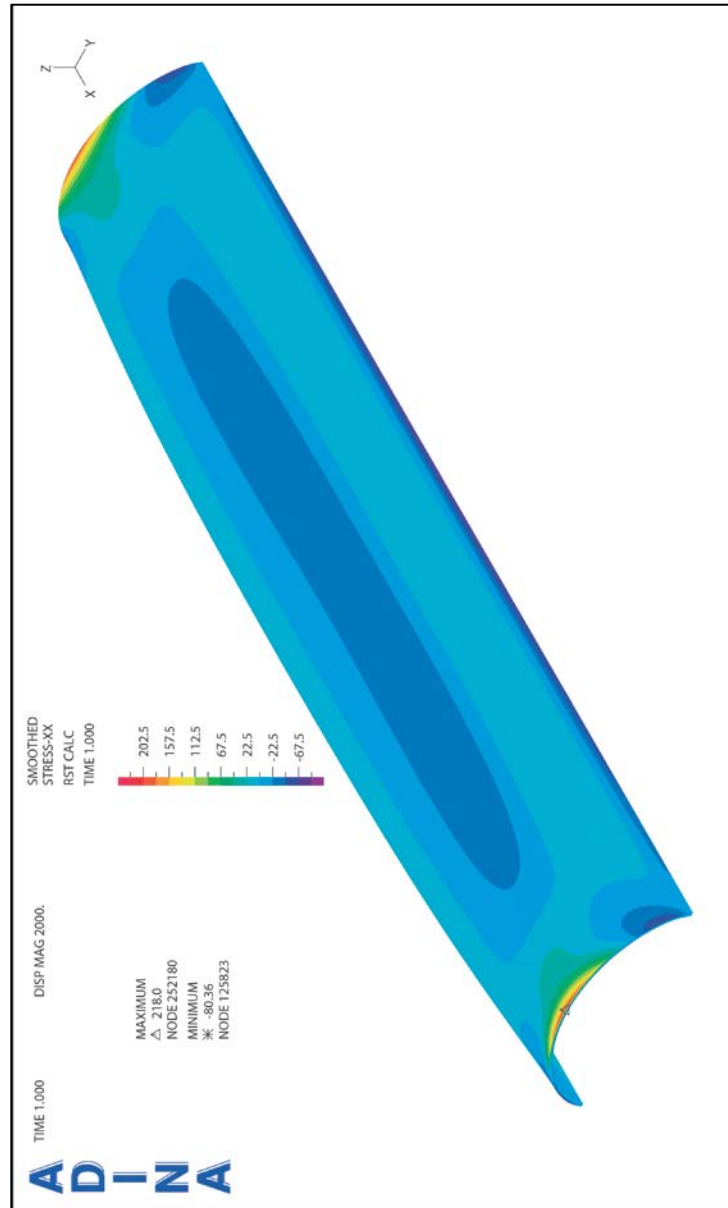
Figure 33. Longitudinal stress on the deformed shape of FEM-6

The deflection of FEM-6 increases very slightly from -0.0258 in. to -0.0265 in. as shown in Figure 34 and thus causes the longitudinal stress at the crown of the shell's mid-surface to also increase from -26.1 psi to -39.5 psi. However, the differences are too

small to be considered significant. The radial stresses stay approximately the same and are shown in Figure 35. These observations lead to a conclusion that stiffening the shell on both ends and edges is an inefficient use of material.
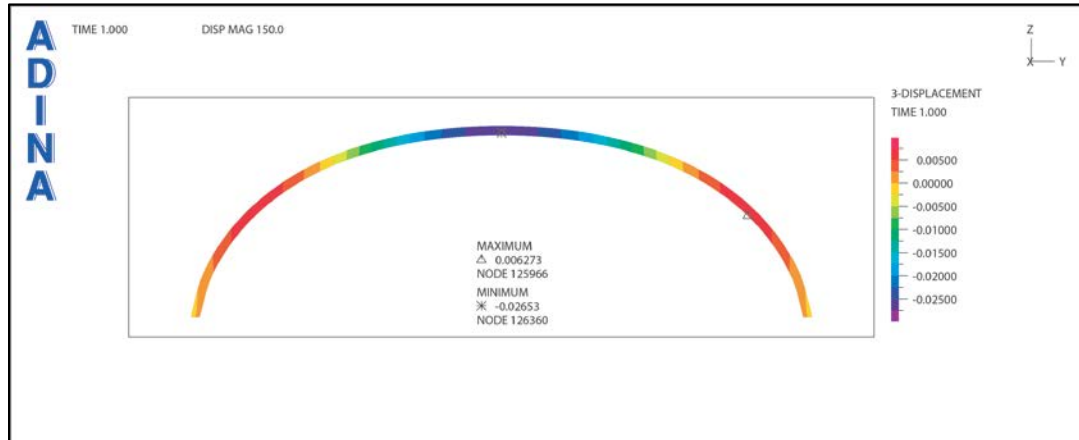

Figure 34. Plot of vertical deflection (in.) at the midspan cross-section of FEM-6
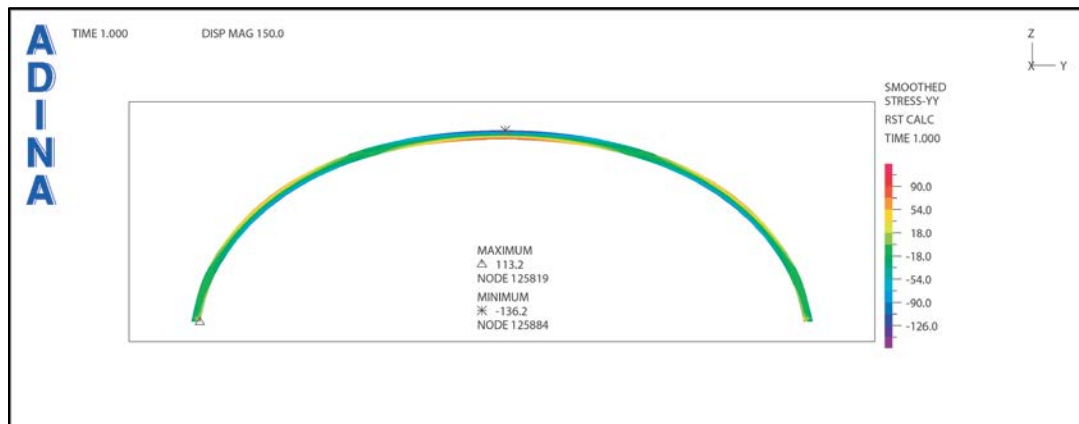

Figure 35. Radial stresses (psi) at the mid-span cross-section of FEM-6

FEM-4 is similar to FEM-1 because FEM-4 also exhibits beam-like behavior, which is shown in Figure 33. The beam-like behavior is most pronounced at the mid-span of the model, where the longitudinal stress changes from compression to tension between

crown and the edge respectively. At the rings, however, tensile longitudinal stress develops at the crown due to the material pulling out of the fixed crown. Compressive stress, on the other hand, develops at the springing due to the fact that translation at the rings is fixed along the *x*-axis.
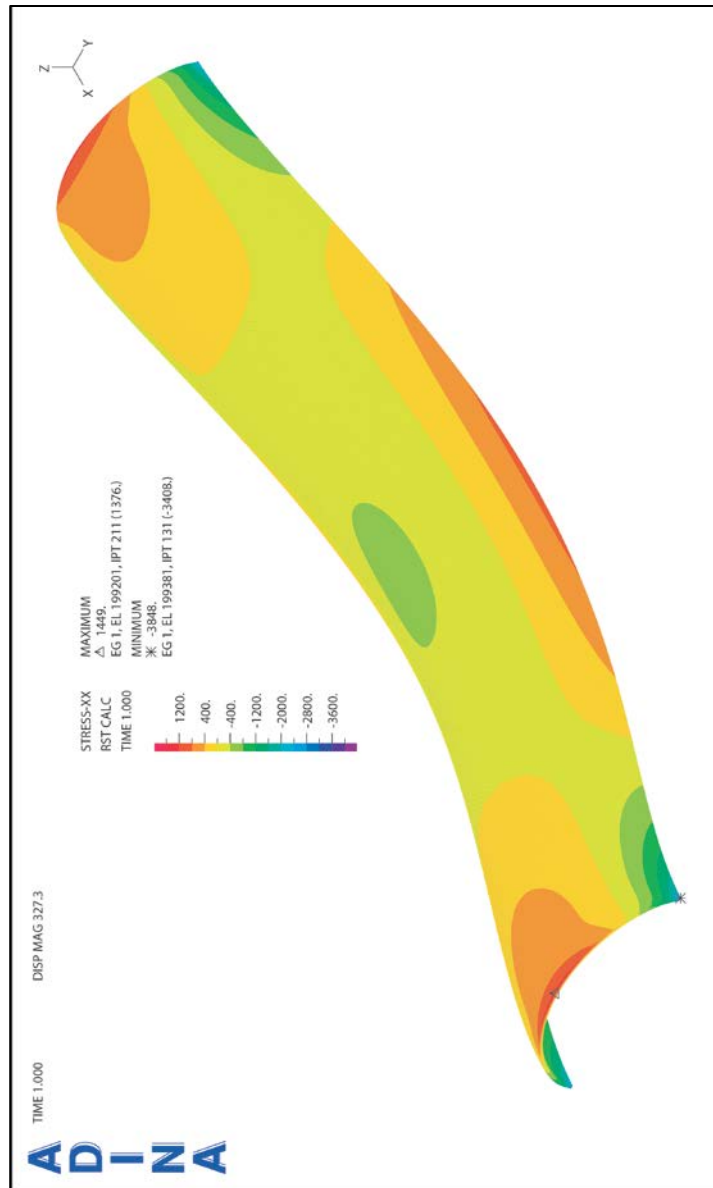

Figure 36. Longitudinal stress on the deformed shape of FEM-3

Rigidly supporting the rings in FEM-4 creates a more efficient structure than FEM-1 in terms of lower deflections and lower stresses. Deflections are reduced to -0.3285 in at the crown and -0.3669 at the edge as shown in Figure 37.
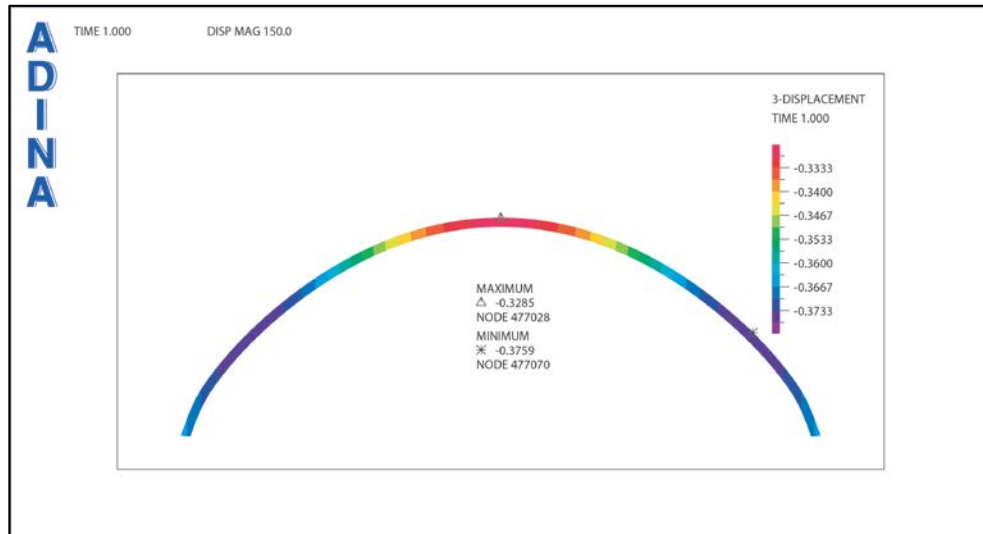

Figure 37. Vertical deflection (in.) at the midspan cross-section of FEM-4

The radial stress on the outside surface of the crown decreased from 138.3 psi (FEM-1) in tension to 112.4 psi (FEM-4) in tension and the radial stress on the inside surface of the crown decreased from -226.6 psi (FEM-1) in compression to -194.5 psi (FEM-4) in compression as shown in Figure 38. However, the radial stress at the mid-surface of the crown increased slightly from -9.47 psi (FEM-1) in compression to -19.9 psi (FEM-4) in compression. The longitudinal stress at the crown dropped to -442.4 psi in compression (FEM-4) as shown in Figure 39. However the tensile stress, although smaller, is still large. The design would have to include reinforcing or prestressing to counteract 929.7

psi of tension at the edge of the structure. This observation leads to the next model that was created and tested.

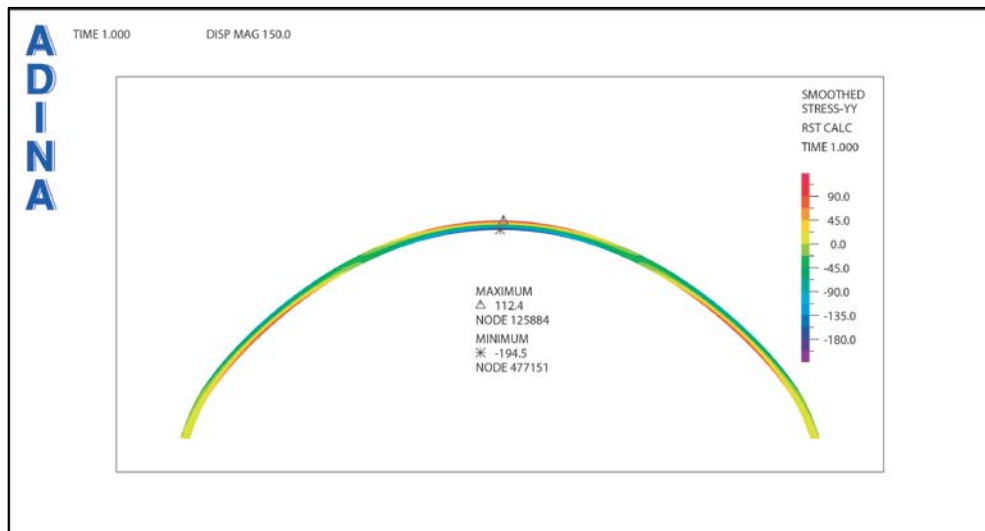**Figure 38. Radial stresses (psi) at the mid-span cross-section of FEM-4**

Figure 39. Longitudinal stresses (psi) at the mid-span cross-section of FEM-4

The use of prestressing yields a significant improvement in the behavior of the shell even without the inclusion of the stiffening ring or edge beams. Prestressing reduced the deflection at the crown from -1.284 in. (FEM-1) to -0.1058 in. (FEM-2) as shown in Figure 40, and the deflection at the edge from -1.328 in. (FEM-1) to -0.104 in. (FEM-2).
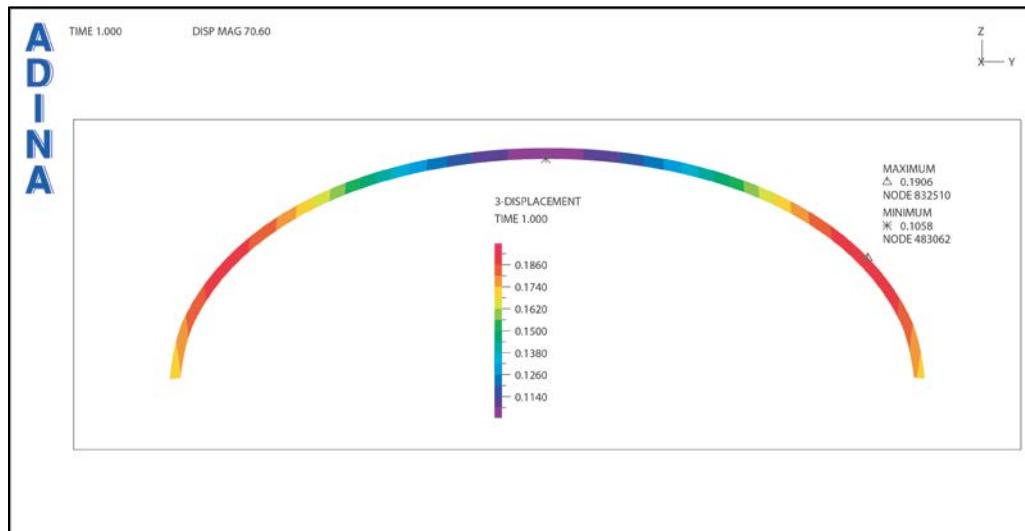

Figure 40. Vertical deflection (in.) at the midspan cross-section of FEM-2

The significant longitudinal tensile stress at the edge was completely counteracted by the use of prestressing, which results in a compressive stress of -1553 psi. The compressive longitudinal stress at the crown was reduced to -372.4 psi. The plot of longitudinal stresses along the entire length of FEM-2 is shown in Figure 41. Figure 41 demonstrates that FEM-2 behaves as a beam, since stress is transferred longitudinally. However, the distribution of stress is irregular mainly due to the shape of prestressing cables. Also, stress irregularities are present in the regions of prestressing anchorage points and support surfaces.
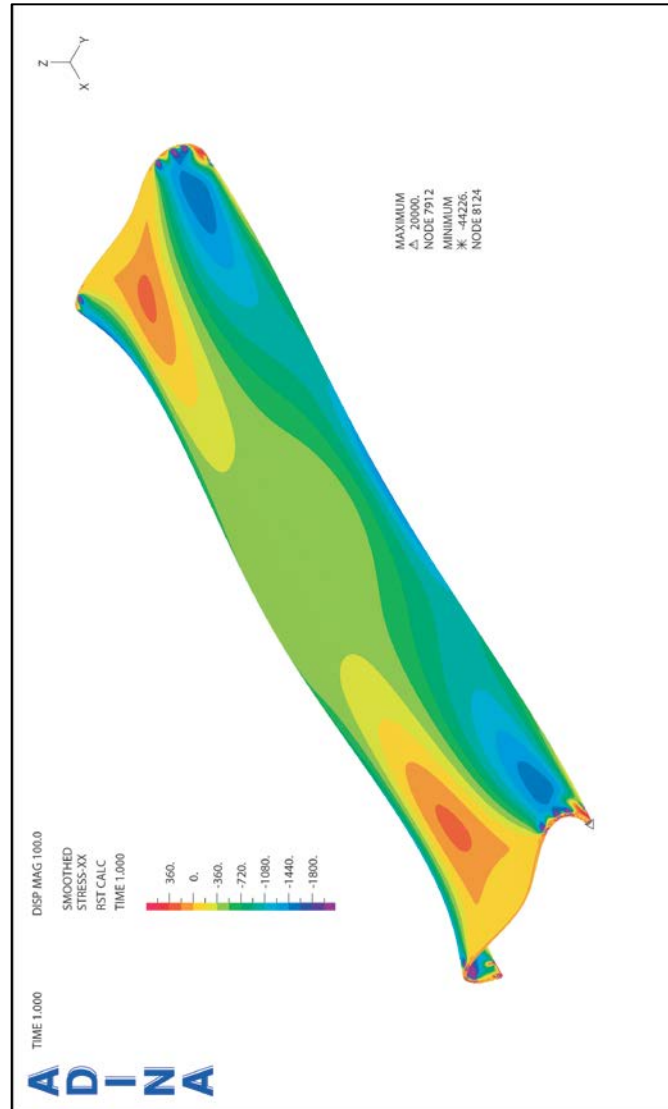
Figure 41. Longitudinal stress on the deformed shape of FEM-2

The plot of radial stresses in presented in Figure 43. Radial stresses change from tension
to compression and increase most noticeably at the outside surface of the crown from
138.3 psi (FEM-1) in tension to -240.2 psi (FEM-2) in compression. In practice, concrete
is designed to carry zero tensile stress unless it is reinforced. Concrete subjected mainly
to compressive stresses is preferred because it requires minimal reinforcing. Thus, the

most significant result of FEM-2 is the transformation of 2179 psi in tension (FEM-1) into -1583 psi in compression.
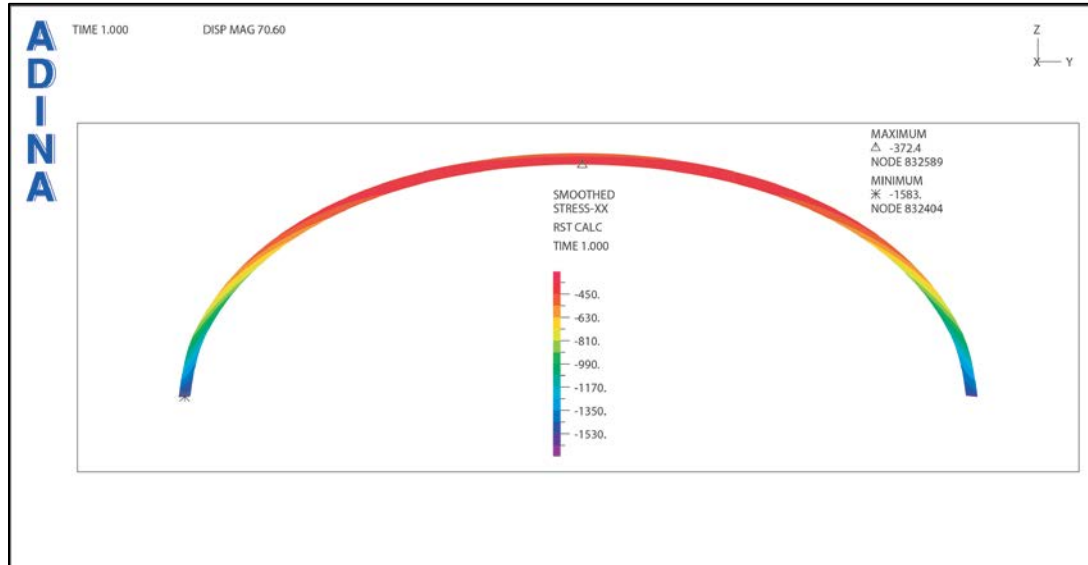

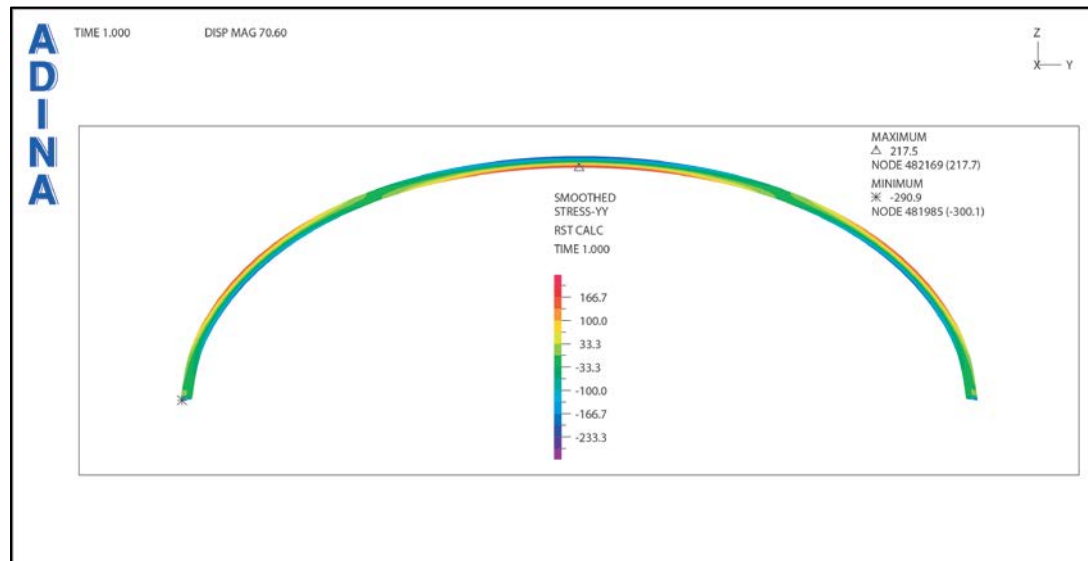**Figure 42. Longitudinal stresses (psi) at the mid-span cross-section of FEM-2**

Figure 43. Radial stresses (psi) at the mid-span cross-section of FEM-2

If the prestressed shell is also fixed at the ring as in FEM-5, the structure's performance improves as compared to FEM-2. The deflection drops from -0.1058 in (FEM-2) to -0.0949 in (FEM-5) at the crown as shown in Figure 45 and from -0.104 in. (FEM-2) to -0.012 in. (FEM-5) at the edge. The beam-like behavior is demonstrated by Figure 44 where stresses are distributed along the length of the shell. The presence of prestressing elevates the middle section of the shell, while letting the remaining two sections sag. Virtually this creates three separate "beams" in terms of the distribution of tensile and compressive stresses.
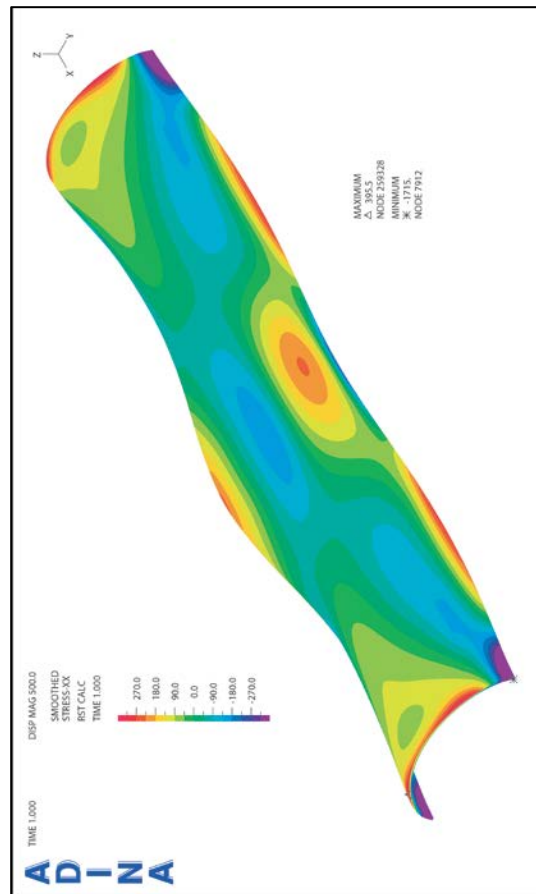

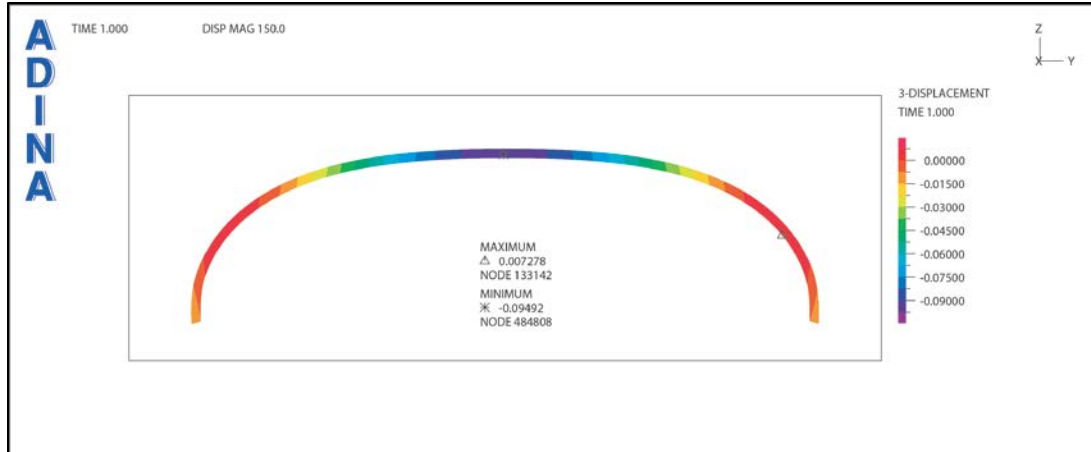**Figure 44. Longitudinal stress on the deformed shape of FEM-5**

Figure 45. Vertical deflection (in.) at the midspan cross-section of FEM-5

The longitudinal compressive stresses become smaller in FEM-5, particularly at the edge of the midspan surface, where the compressive stress drops from -1553 psi (FEM-2) to -946 psi (FEM-5) as shown in Figure 46. However, the radial stresses increase slightly in FEM-5. The radial stress on the outside surface increases to -292.4 psi while the radial stress on the inside surface increases to 274.8 psi as shown in Figure 47.

Figure 46. Longitudinal stresses (psi) at the mid-span cross-section of FEM-5
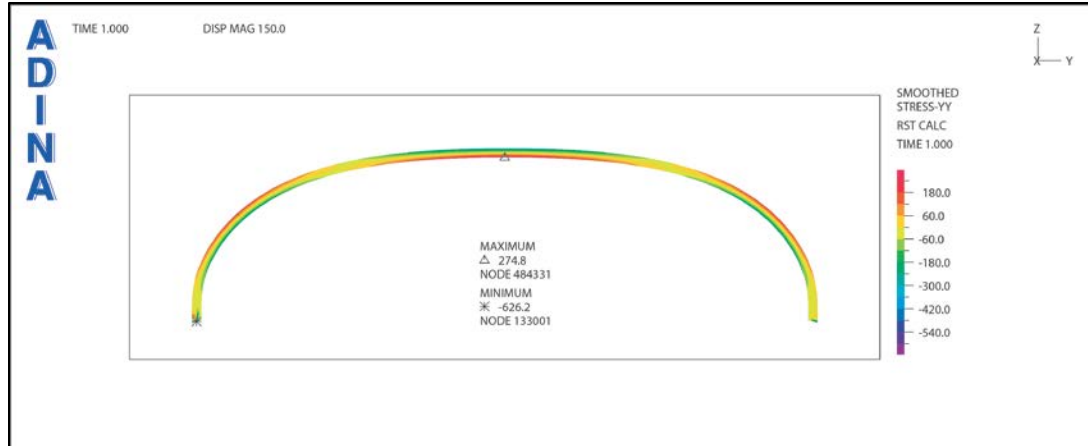
Figure 47. Radial stresses (psi) at the mid-span cross-section of FEM-5

FEM-7 was the first out of two most realistic models, which utilized stiffening rings and edge beams. FEM-7 served to determine whether the use of prestressing is necessary together with the edge and ring beams. The deflection of FEM-7 is lower when compared to FEM-1 (-0.4682 in. vs. -1.284 in. at the crown as shown in Figure 48 and -0.5044 in. vs. -1.328 in. at the edge).
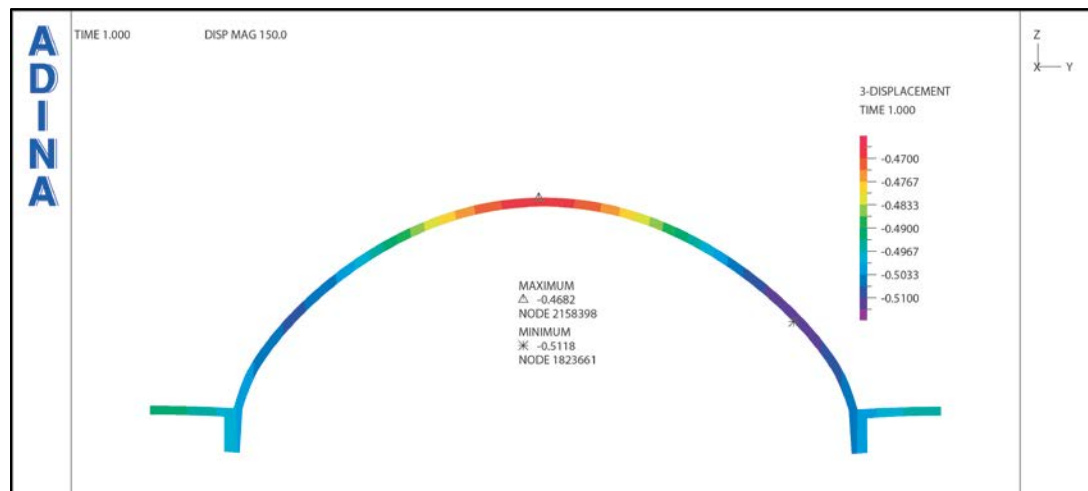

Figure 48. Vertical deflection (in.) at the midspan cross-section of FEM-7

The longitudinal compressive stress at the crown was reduced -1141 psi (FEM-1) to -742.4 psi (FEM-7) and the tension stress was reduced from 2179 psi (FEM-1) to 996.4 psi (FEM-7) as shown in Figure 50. It is important to note that without the use of prestressing, the structure develops tensile stress. The deflected shape remained similar to the one in FEM-1 and the beam-like behavior was preserved as shown in Figure 49. Unusual patches of tensile stress were observed at the corners of FEM-7; however their presence does not noticeably affect the stress distribution at the mid-span according to Saint-Venant's Principle because of a large distance between the irregular stress distribution at the corners and the mid-span.
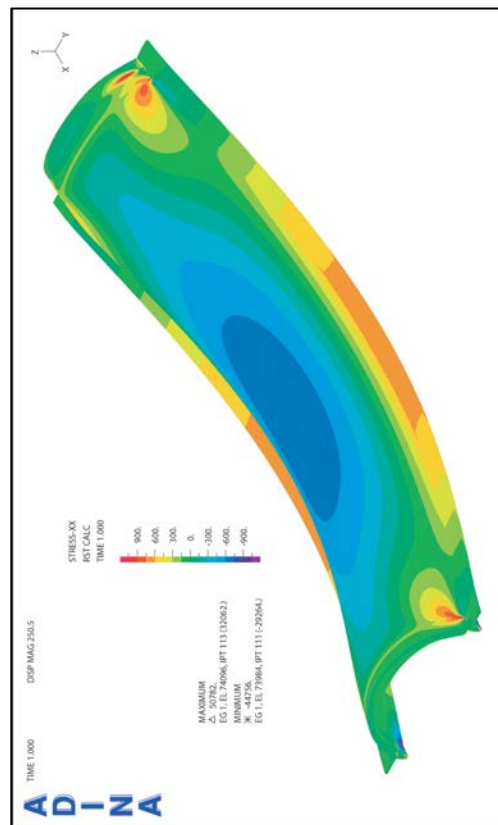

Figure 49. Longitudinal stress on the deformed shape of FEM-7

The radial stresses, however, dropped from 138.3 psi (FEM-1) to 88.2 psi (FEM-7) at the outside surface of the crown and from -226.6 psi (FEM-1) to -166.9 psi (FEM-7) at the inside surface as shown in Figure 40. The stress at the mid-surface of the crown increased from -9.47 psi (FEM-1) to -37.4 psi (FEM-7). However, the performance of FEM-7 does not compare well with FEM-5. The radial stresses are lower in FEM-7, but the deflections and the longitudinal stresses are lower in FEM-5. It is important to note the absence of any tension in the longitudinal direction in FEM-5.
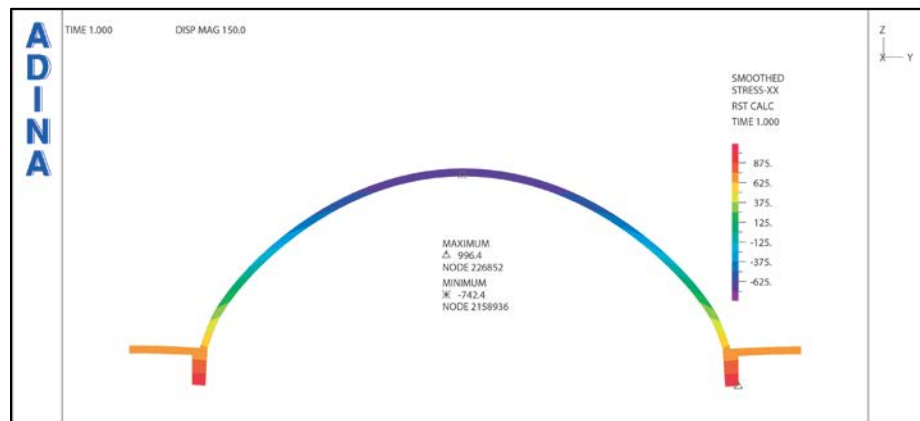

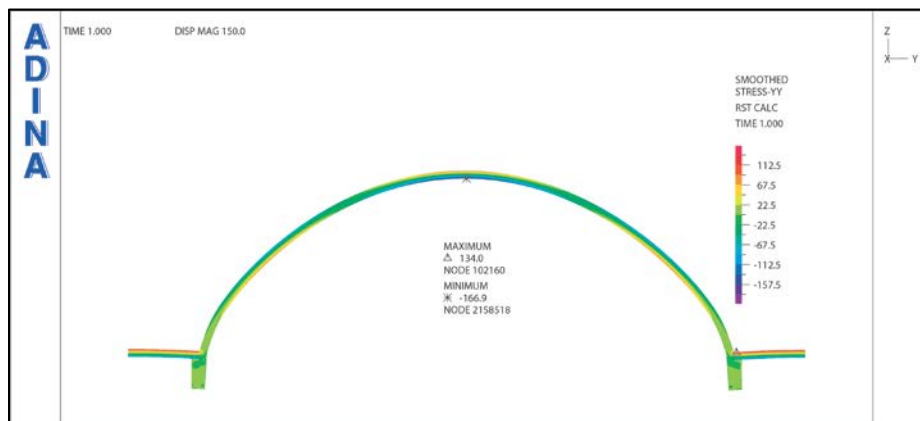**Figure 50. Longitudinal stresses (psi) at the mid-span cross-section of FEM-7**

Figure 51. Radial stresses (psi) at the mid-span cross-section of FEM-7

The addition of prestressing in model FEM-8, however, makes a significant improvement in performance. The deflections at the crown and the edge of FEM-8 are closer to the ones in FEM-5 with -0.1739 in. at the crown as shown in Figure 53 and -0.1485 in. at the edge. The beam-like behavior is demonstrated in Figure 50. The irregular stress distribution was caused by the anchorage zone of the prestressing cables.
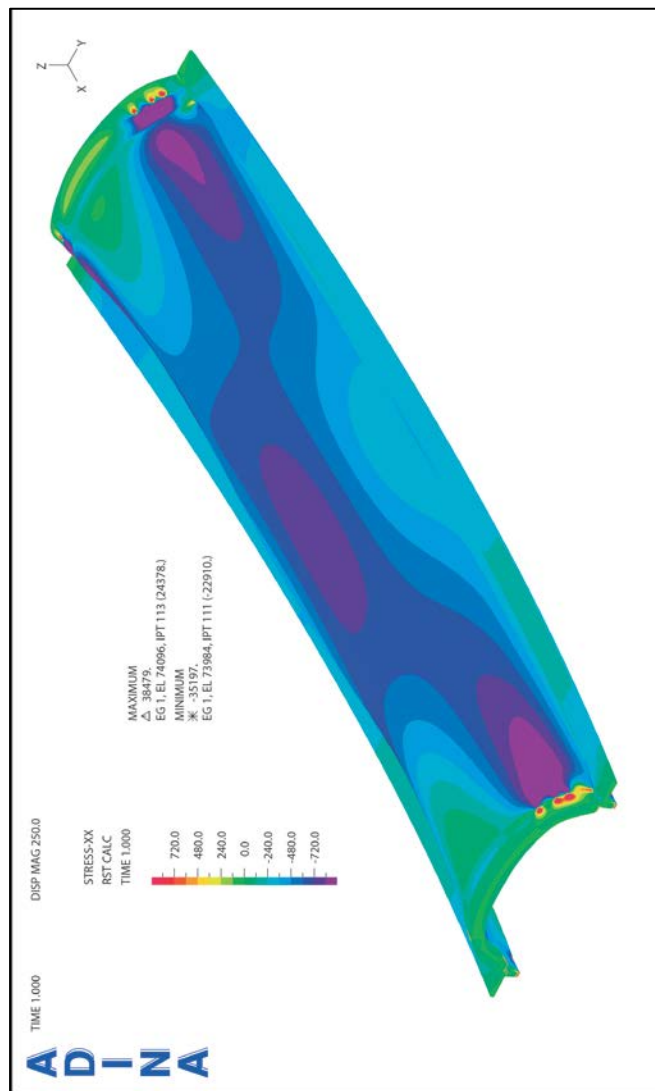
Figure 52. Longitudinal stress on the deformed shape of FEM-8
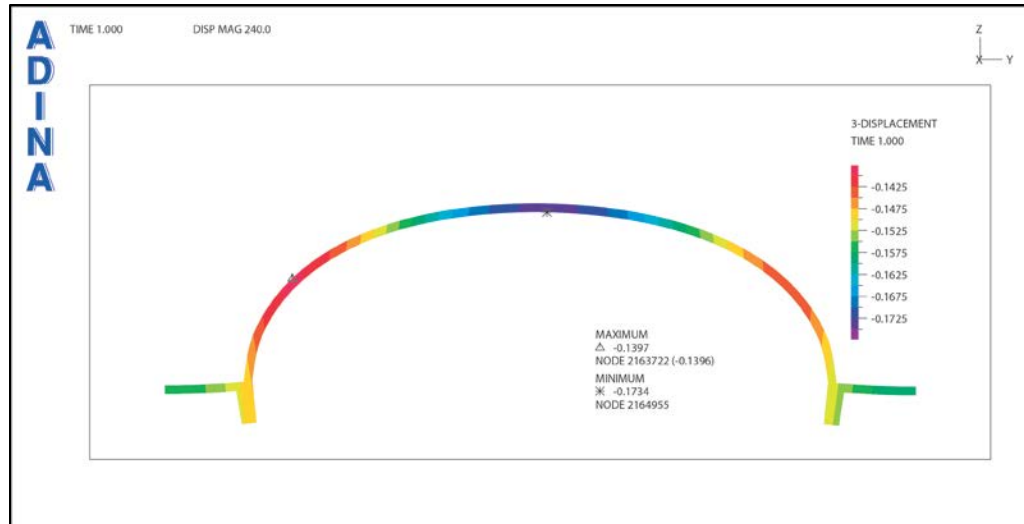
Figure 53. Vertical deflection (in.) at the midspan cross-section of FEM-8

Due to the use of prestressing the longitudinal tensile stress of FEM-7 was counteracted and transformed into -346.6 psi compressive stress. The change in radial stress between FEM-7 and FEM-8 was not significant. The distribution of longitudinal and radial stresses is presented in Figure 54 and Figure 55 respectively.

Figure 54. Longitudinal stresses (psi) at the mid-span cross-section of FEM-8

Figure 55. Radial stresses (psi) at the mid-span cross-section of FEM-8

As mentioned in the previous chapter, FEM-8, being the most realistic model, was compared with Komendant's calculations. The 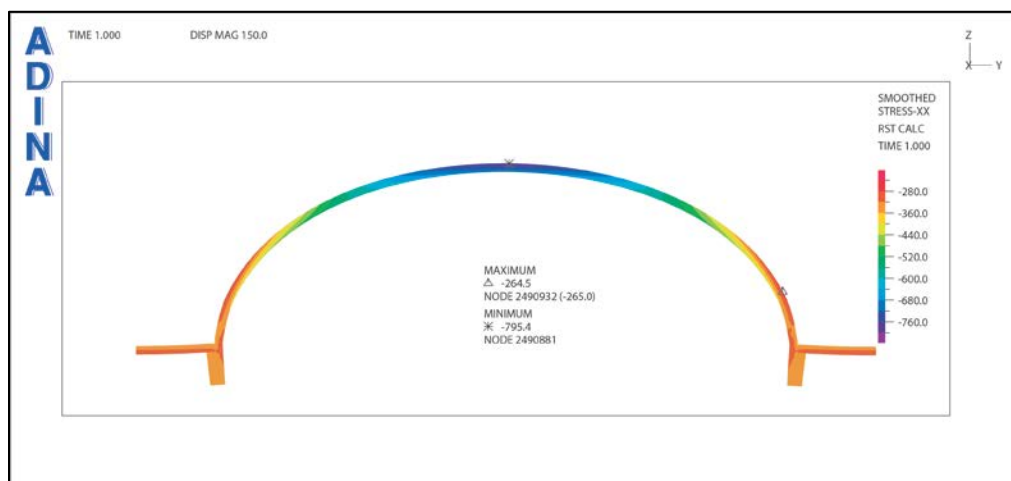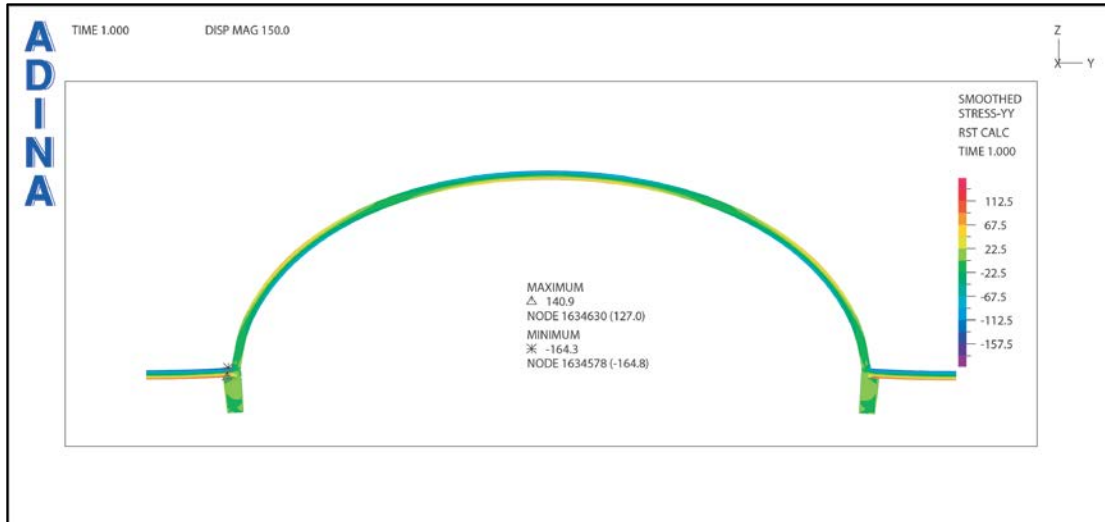first criterion for comparison was the values of deflection. The effects of creep and shrinkage were not modeled on the material level, however the final prestressing strain at $t=n$ was applied. The maximum deflection of -0.1739 in. that was found in FEM-8 was compared to the Komendant's value of deflection and was found to be larger than Komendant's deflection at $t=0$ (-0.152 in.) but smaller than his prediction at $t=n$ (-0.3814 in.). Komendant predicted larger longitudinal stress of -903 psi at the crown (vs. -796.7 psi in FEM-8) and 37 psi at the edge (vs. -346.5 psi in FEM-8). Finally, Komendant's values of radial stress were found to be smaller than in FEM-8. The model predicts -125.5 psi at the top of the crown and 82.9 psi at the bottom. The axial component of stress in Komendant's calculations was neglected as mentioned in Chapter 4.1, which resulted in 39.4 psi in tension at the bottom and -39.4

psi in compression at the top. Again, considering the strength of concrete of 5000 psi, the

difference in stress is negligible. All aforementioned values are summarized in Table 6.

Table 6. Comparison of Komendant's calculations to the results of FEM-8

Komendant			FEM-8	
Initial total deflection (in)	-0.152		Maximum deflection (in)	-0.1739
Final total deflection (in)	-0.3814			
Final longitudinal stress with PT at crown (psi)	-903		Longitudinal stress at crown (psi)	-796.7
Final longitudinal stress with PT at edge (psi)	37		Longitudinal stress at edge (psi)	-346.5
Radial stress at the top of crown due to loads and PT (psi)	-39.4		Radial stress at the top of crown (psi)	-125.5
Radial stress at the bottom of crown due to loads and PT (psi)	39.4		Radial stress at the bottom of crown (psi)	82.9

A number of factors contributed to the difference between the results of the FEM

analyses and Komendant's calculations. A review of Komendant's calculations showed

that he was primarily concerned with what he considered to be the worst case. However,

understanding the exact behavior of the assembly is critical is achieving an efficient

structure. The analysis that was carried out in ADINA showed a shell behavior that could

be hard to imagine and visualize. The most complex model, FEM-8 does behave as a

beam but there are several details that should be accounted for. It was shown that the

deflection actually differs between the crown and the edge. The deflection along the

length of the shell also varies. Due to the distortion of the cross-section, it does not follow

a smooth concave up shape as could be predicted by following a beam analogy. On the

contrary, along its length the shell starts as concave down, which gradually turns into concave up and lastly ends with concave down again. The difference between the values obtained from ADINA and the ones calculated by Komendant also resulted from his approach to the analysis. From the first page of his calculations where he described and calculated the geometric properties of the cycloid, he subdivided it only into 11 segments over an approximately 23 ft. span. The cycloid part of the ADINA model included 50 points equally spread over the span of the cycloid. All of the aforementioned factors contributed to the difference in data.

Chapter 5: Conclusion

Today's technology of finite element analysis allows a designer to understand a structure to a much higher degree of detail. Finite element analysis allows for a more accurate understanding of the behavior of the structure under a set of loads and constraints and suggests an appropriate solution. FEM analysis of the shells of Kimbell Art Museum were used to investigate the effectiveness of the ring beams, edge beams and prestressing and form a new perspective on Komendant's design. The results of the most realistic model, FEM-8 were found to be close to Komendant's calculations, which suggests the validity of linear elastic analysis and the choice of element type. The difference in calculations could have been caused primarily due to Komendant's choice of subdivisions as described in Chapter 5.

From the analysis it was determined that both FEM-5 and FEM-8 can be successfully and effectively implemented in practice. Prestressing was used in both models and thus served as the main contribution to efficiency. FEM-5 showed that ring and edge beams can be avoided, however an architect might find them more aesthetically appropriate than rigid walls as was the case in Kimbell Art Museum. Even though Komendant's design might have not produced the most economical structure it definitely produced a structure that worked and fit within the limits of Louis Kahn's monumental and monolithic architectural style. The combination of Komendant's approach to design and Kahn's belief in the monumental architecture yielded a historical structure that stimulated the minds and aspirations of future generations of engineers and architects.

Chapter 6: Future Work

Several additional aspects of Kimbell Art Museum are important to look at. Future work will include taking a closer look at the effect of prestressing on the longitudinal stresses of the shells. Theoretically, the prestressing is capable of eliminating the tensile stresses, which increases the efficiency of concrete. However, the geometry of the shells makes this objective very hard to achieve. Thus, it is important to study the longitudinal stresses on the outside, inside and mid-surface of the shell caused by the prestressing force.

Another interesting aspect of Kimbell Art Museum is the connection between structure and architecture. The thickness and location of the ring beams contributes to the monumental appeal of the structure, however it visually obstructs the thinness of the shell and, as a result, the efficiency stays hidden to an observer. Therefore, Komendant could have chosen to design a much thicker shell. This interaction between structure and architecture requires some further study.

Finally, future work will review the history of the Kimbell Art Museum and its relation to other shell structures. Other examples of thin shells will be presented and compared to the Kimbell Art Museum. The findings will put the roof designs of August Komendant in proper historical and technical perspective.

Bibliography

1. ADINA R & D, Inc. (2011). Theory and modeling guide, volume 1: ADINA solids & structures.

2. American Concrete Institute. (2011). *Building code requirements for structural concrete (ACI 318-08) and commentary*. American Concrete Institute.

3. Billington, D. P. (1976). Historical Perspective on Prestressed Concrete. *PCI Journal*, Retrieved from

   http://www.pci.org/pdf/publications/journal/2004/January-February/JL-04-JANUARY-FEBRUARY-1.pdf

4. Bess of both worlds: Architecture. (2013). Retrieved from
   http://bessandmatt.wordpress.com/category/architecture/

5. Charleson, A. W., & Pirie, S. (2009). An Investigation of Structural Engineer-Architect Collaboration. *Journal of the Structural Engineering Society*, 22(1), 97-104. Retrieved from http://www.curee.org/architecture/docs/img-917144039-0001.pdf

6. Heyman, J. (1977). *Equilibrium in shell structures*. East Kilbride, Great Britain: Thomson Litho Ltd.

7. Highsmith, C. M. (2011). Kimbell Art Museum. Retrieved from
   http://en.wikipedia.org/wiki/File:Kimbell_Art_Museum_Highsmith.jpg

8. Hines, E. M., & Billington, D. P. (2004). Anton Tedesko and the Introduction of Thin Shell Concrete Roofs in the United States. *Journal of Structural Engineering*, 1639-1650.

9.   Kimbell Art Museum. (2014). Kimbell Art Museum: Light. Retrieved from https://www.kimbellart.org/architecture/kahn-building/light

10.   Komendant, A. (1972). *Contemporary concrete structures*. McGraw-Hill.

11.   Komendant, A. E. (1987). *Practical structural analysis for architectural engineering*. Englewood Cliffs, NJ: Prentice - Hall, Inc.

12.   Komendant, A. (1952). *Pre-stressed concrete structures*. McGraw-Hill.

13.   Komendant, A. (1972). *Statical computations: Stress & deformation analysis*. Archives of the University of Pennsylvania

14.   Komendant, A. (1975). *18 years with Architect Louis I. Kahn*.

15.   Leslie, T. (2005). *Louis I. Kahn: Building art, building science*. New York: George Braziller, Inc.

16.   Lin, T. Y., Kulka, F., & Lo, K. (1973). Giant Prestressed HP Shell for Ponce Coliseum. *PCI Journal*, Retrieved from http://www.pci.org/view_file.cfm?file=JL-73-SEPTEMBER-OCTOBER-5.pdf

17.   The Louis I. Kahn Collection, The Architectural Archives of the University of Pennsylvania. Retrieved from: http://www.design.upenn.edu/archives/majorcollections/kahn/likidxname.html

18.   Nordenson, G. (2004). Lo Sviluppo delle strutture e il Kimbell Art Museum. The lineage of structure and the Kimbell Art Museum. Lotus International

19.   Paya-Zaforteza, I., & Lozano-Galant, J. A. (2011). Structural Analysis of Eduardo Torroja's Fronton de Recoletos' Roof. *Engineering Structures 33*, (3)

20. Pfluger, A. (1961). *Elementary statics in shells*. (2nd ed.). New York: F. W. Dodge Corporation.

21. Praefcke, A. W. (2009, October). Kimbell Art Museum Fort Worth. Retrieved from http://en.wikipedia.org/wiki/File:Kimbell_Art_Museum_Fort_Worth_02.jpg

22. Roark, R. J. (1989). *Formulas for stress and strain*. (4th ed.). McGraw Hill.

23. University of Pennsylvania. (2009). Louis Kahn: The making of a room. Retrieved from http://www.arthistory.upenn.edu/themakingofaroom/catalogue/section7.htm

24. Vimeo. (2012). Kimbell Art Museum, Fort Worth, Texas. Retrieved from http://vimeo.com/25365638

25. WolframMathworld (2014). *Cycloid*. Retrieved from http://mathworld.wolfram.com/Cycloid.html

Appendix A
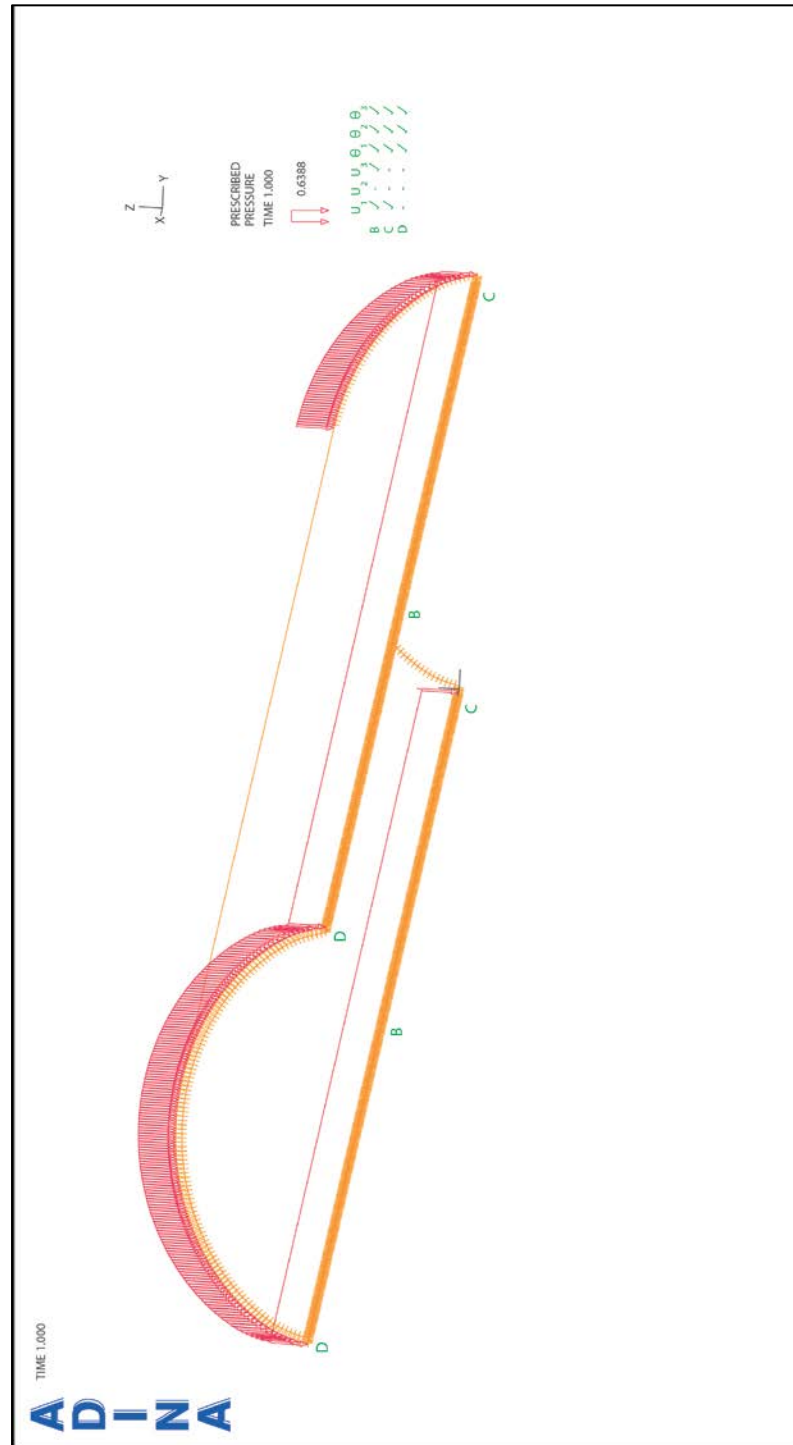
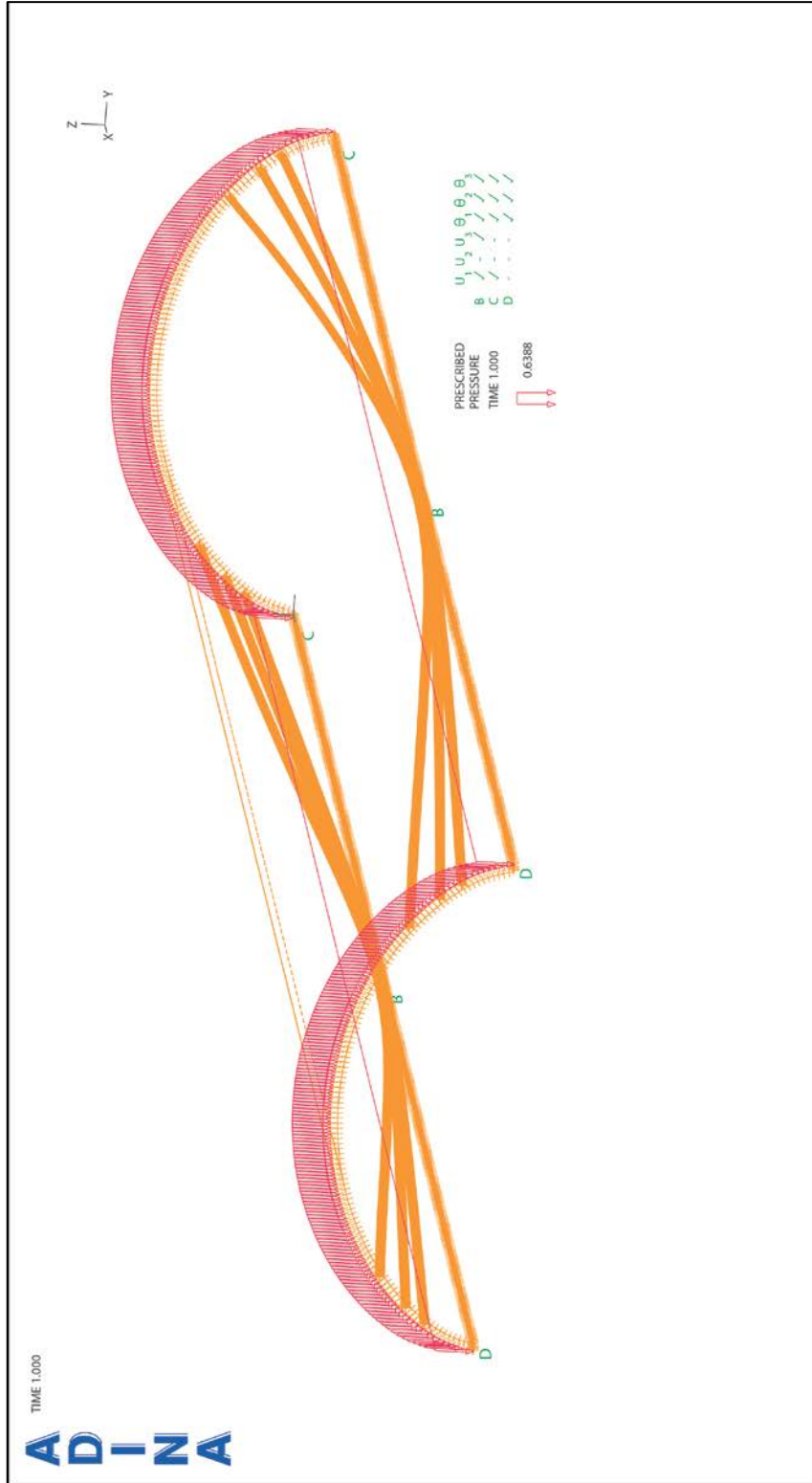**Figure 56. FEM-1, geometry, boundary conditions, loading**

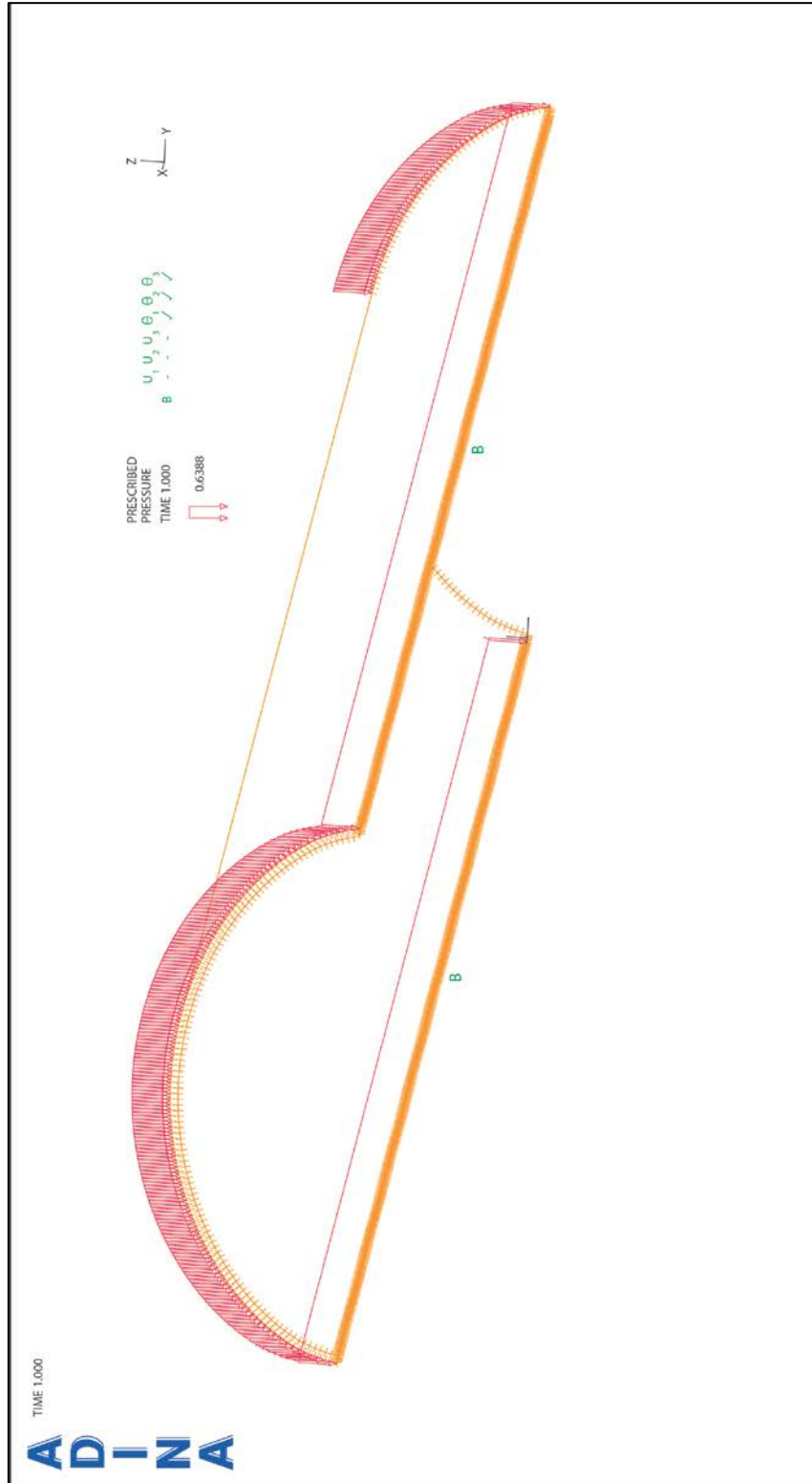**Figure 57. FEM-2, geometry, boundary conditions, loading**

71

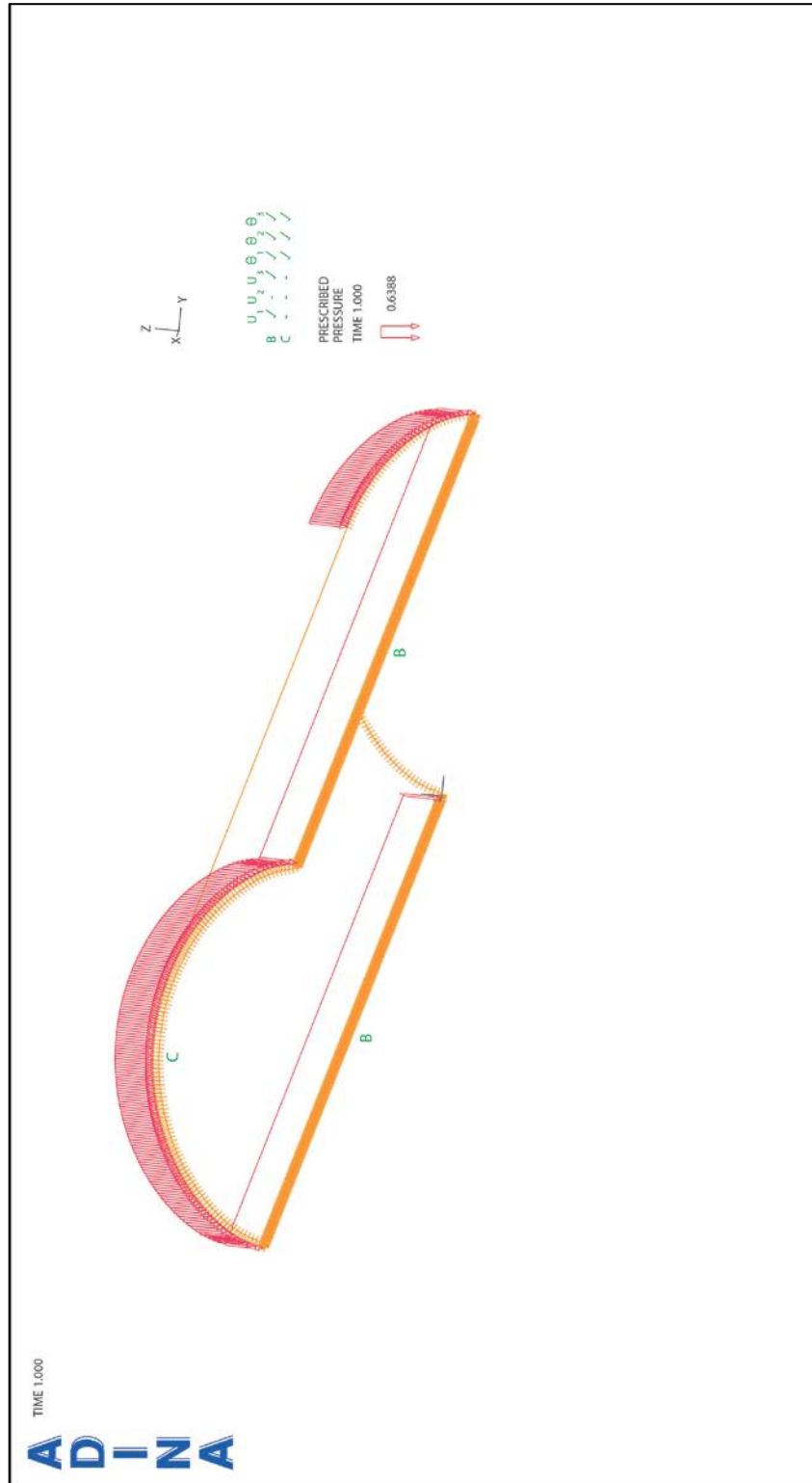**Figure 58. FEM-3, geometry, boundary conditions, loading**

Figure 59. FEM-4, geometry, boundary conditions, loading

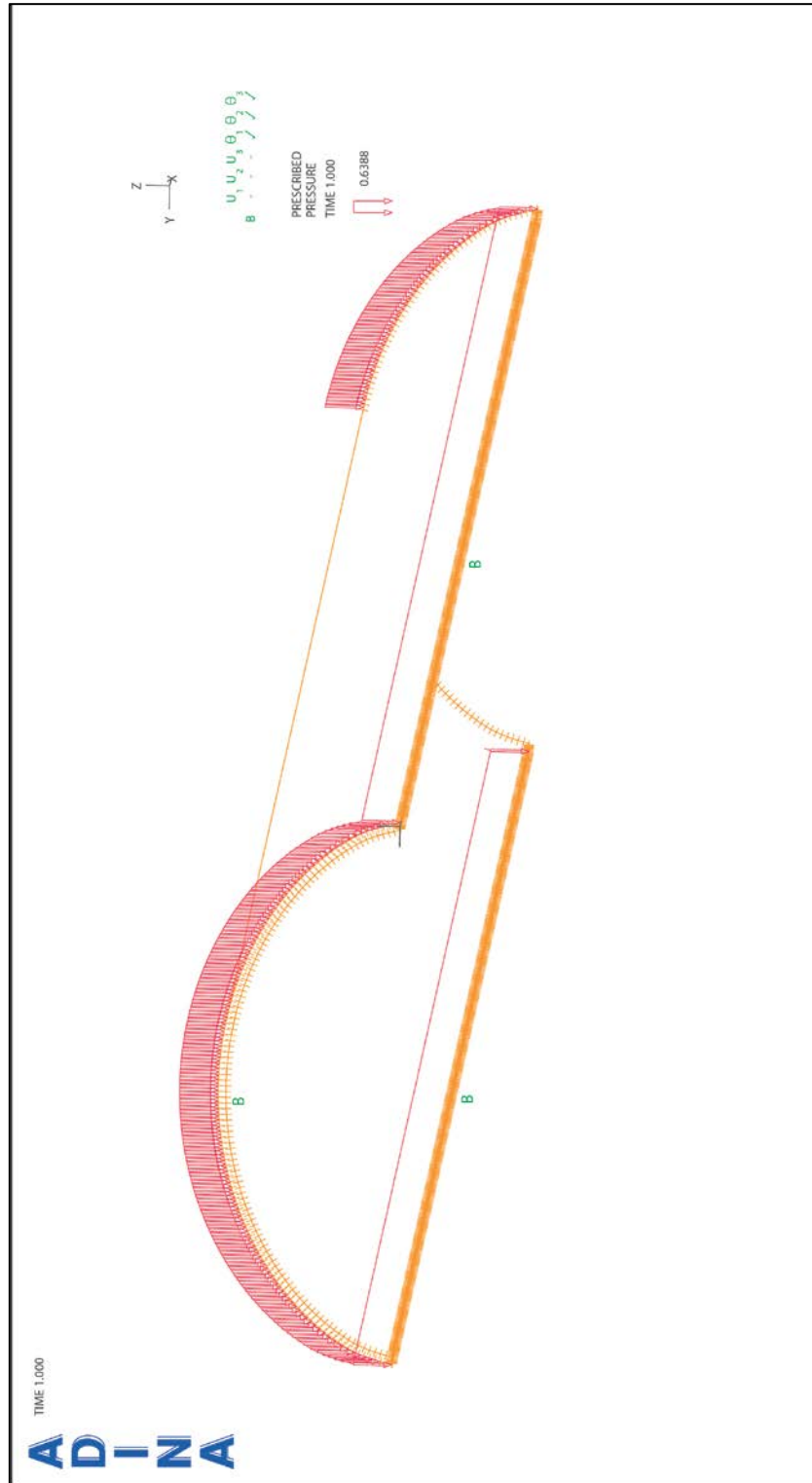**Figure 60. FEM-5, geometry, boundary conditions, loading**

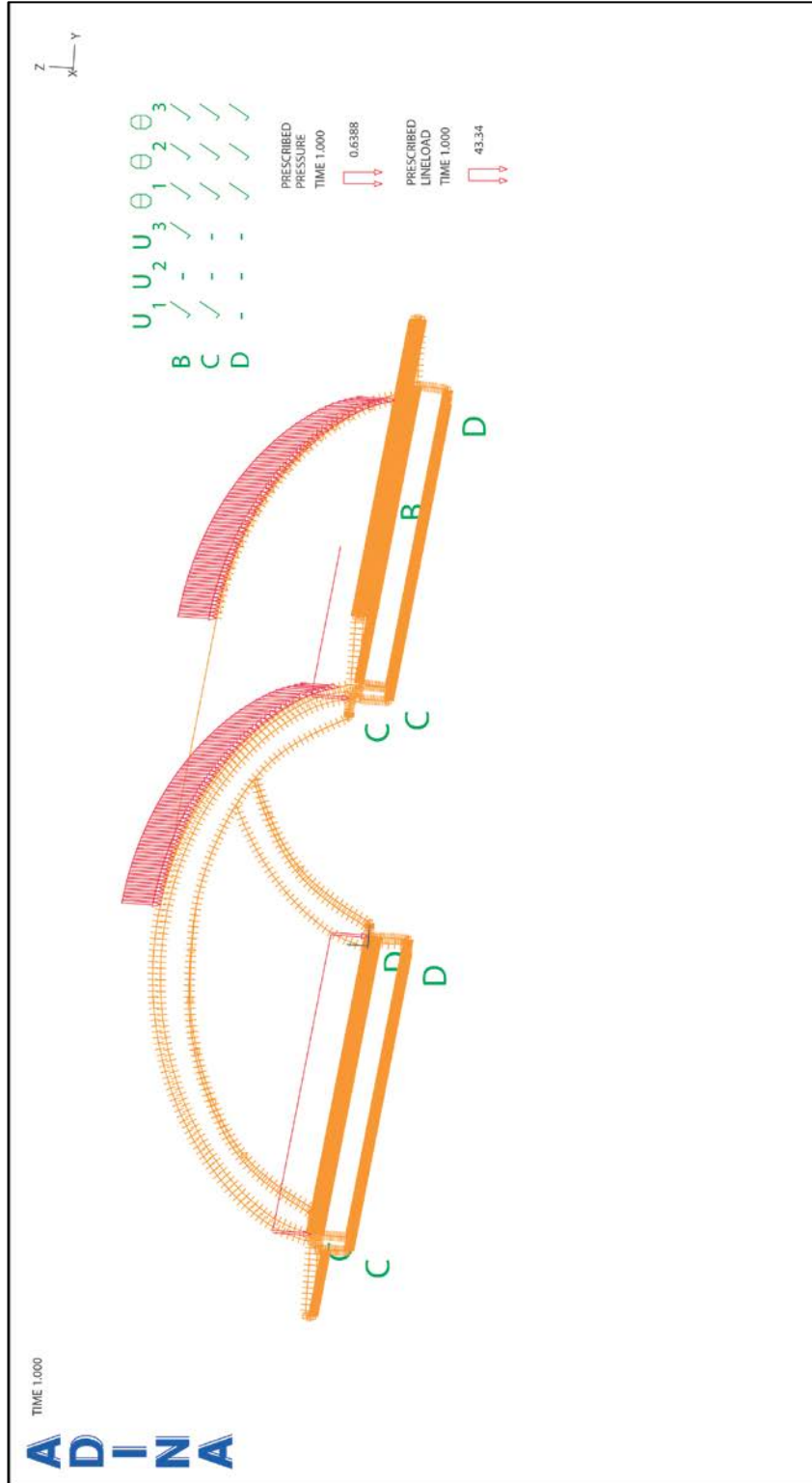**Figure 61. FEM-6, geometry, boundary conditions, loading**

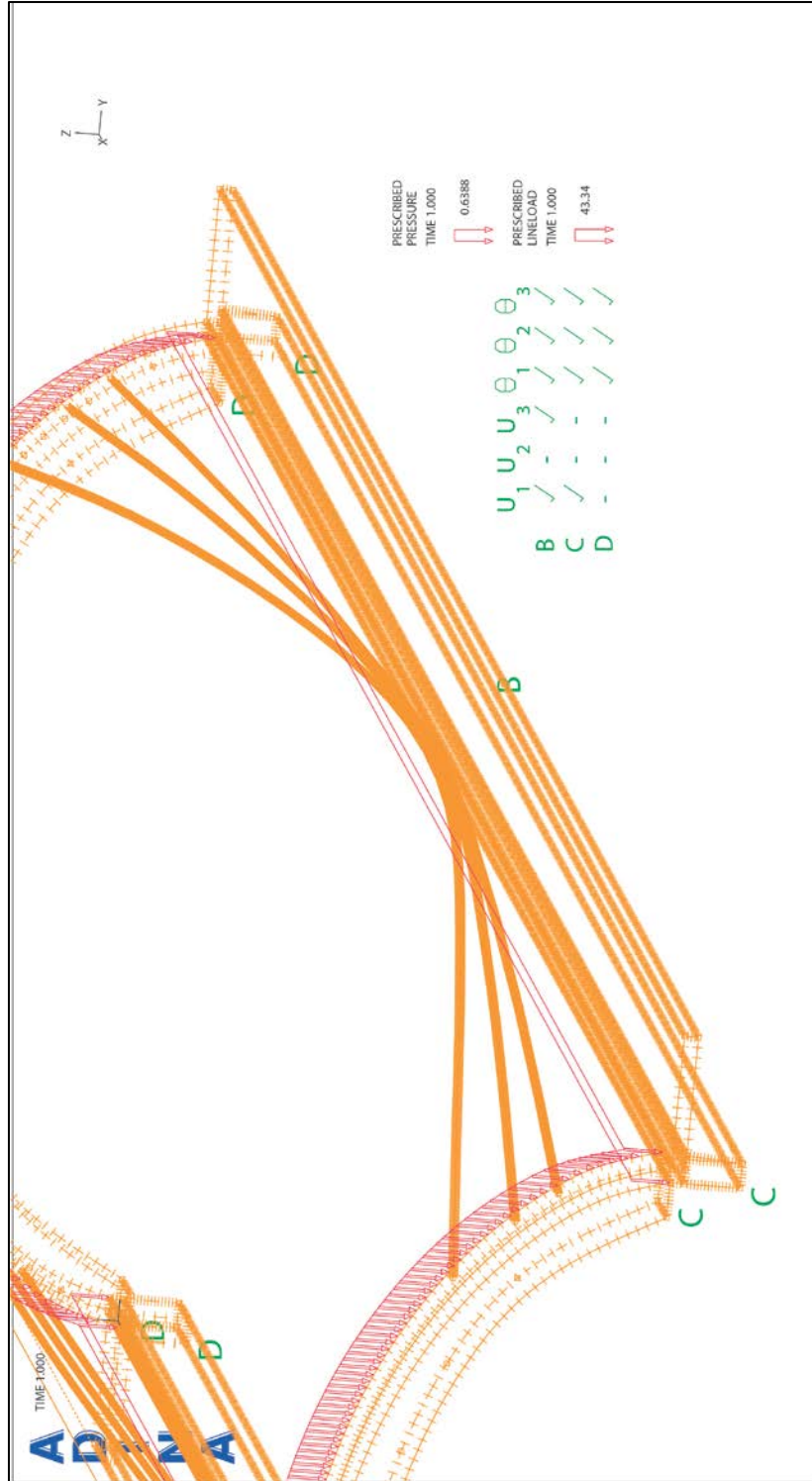**Figure 62. FEM-7, geometry, boundary conditions, loading**

Figure 63. FEM-8 zoomed in, geometry, boundary conditions, loading